TECHNISCHE UNIVERSITÄT WIEN

INSTITUT FÜR PHOTONIK
Photonics Institute

DIPLOMARBEIT

Time-resolved XUV photoelectron-photoion coincidence spectroscopy

zur Erlangung des akademischen Grades

Diplom-Ingenieur

im Rahmen des Studiums

Technische Physik

eingereicht von

Vinzenz Stummer
Matrikelnummer 01125138

ausgeführt am Institut für Photonik
der Fakultät für Elektrotechnik und Informationstechnik der Technischen Universität Wien

Betreuung
Hauptbetreuer: Univ. Prof. PhD Andrius Baltuška
Mitbetreuer: Senior Scientist Dipl.-Ing. Dr. techn. Markus Kitzler-Zeiler

Wien, 08.05.2018

(Unterschrift Verfasser) (Unterschrift Betreuer)

Acknowledgments

I would like to express my gratitude to Andrius Baltuška and Markus Kitzler for their reliable supervision and for introducing me to their fascinating research.
Also, I would like to thank Martin Kirchner and Paolo Carpeggiani for an excellent and cooperative collaboration, Vaclav Hanus for providing parts of his program "Splittex" in addition to useful help in programming and Tobias Flöry for helpful, electronic advises.
Special thanks goes to Ao. Univ. Prof. Dipl. Ing. Dr. techn. Johann Ertl, who helped us a lot with his wide knowledge in electronics and to Assoc.Prof. Dipl.-Ing. Dr.techn. Holger Arthaber.
Last but not least, I would to thank my family for supporting me in all ways possible.

Contents

1 Introduction

The possibility to produce ultrashort light pulses with pulse durations in the femtosecond and attosecond time scale (currently even down to a pulse length of $43as$ [1]) has triggered a worldwide effort of research on time-resolved measurements of electronic dynamics [2, 3, 4] in atoms, molecules [5] and, since very recently, even in solids [6]. For molecules, restructuring of the electronic system induces nuclear dynamics such as the breakage of a chemical bond, which is the primary process of any chemical reaction. In order to study processes like photoionization or photodissociation, measurement techniques needed to be developed, giving us more insight into those processes. One such technique is Photoelectron-Photoion Coincidence Spectroscopy (PEPICO) where the energies of electrons and the mass-to-charge ratio of ions emerging from the interaction of a molecule with an ultrashort light pulse are measured in coincidence. This approach adopted in a time-resolved manner to a pump-probe scheme has already shown great results like direct observation of photochemical activation energy in acetone [7], discovering electronic shake-up in molecular fragmentation processes [8] or the detection of Feshbach resonances [9].

The motivation for this diploma thesis is the effort to implement and test the possibility for PEPICO measurements in an attosecond XUV beamline equipped with a single time-of-flight mass spectrometer. The implementation was enabled by developing a fast high-voltage electrical switch, which permits switching from 0 to $2kV$ within a sub-100 nanosecond duration synchronously with the kHz repetition rate of the laser pulse used for PEPICO measurements, and by developing a suitable software for triggering, data read-out and data visualization during the experiment.

This thesis is divided into the following parts:

- An introduction to PEPICO spectroscopy of molecules
- Description of the measurement setup
- Principle of operation of the fast high-voltage electrical switch
- Presentation of the PEPICO software
- Experimental results
- Conclusions

2 Photoelectron-Photoion Coincidence Spectroscopy of molecules

The generation of ultrashort laser pulses is explained in ch. 2.1. Ch. 2.2 is dedicated to time-resolved photoelectron spectroscopy (TRPES) of molecules. Finally, the way of performing PEPICO measurements with a single time-of-flight spectrometer and its benefits will be explained in ch. 2.3.

2.1 Generation of ultrashort laser pulses in the VIS/IR- and XUV-regime

In order to resolve electronic dynamics, pulse durations in the order of the time scale of such dynamics are needed, which is maximally in the order of a few femtoseconds. So broadband pulses are needed. Additionally, high photon energies are needed for directly accessing deeply bound states or to reach highly excited states. While VIS/IR-pulses show limitations regarding their pulse duration, which is typically tens of femtoseconds, and their photon energy, which is limited up to $\approx 3eV$, XUV pulses overcome these limitations. XUV pulses can be produced with High Harmonic Generation (HHG).

2.1.1 Generation of ultrashort mJ IR pulses

According to Fourier's theorem, which states

$$\Delta t \propto \frac{1}{\Delta\omega} \tag{2.1}$$

for the pulse width Δt of isolated signals with a bandwidth of $\Delta\omega$, a laser which emits spectrally broadband light is needed in order to get short pulses. A very famous candidate for this is the Ti:Sapphire laser, which is a solid state laser where titanium doped sapphire is used as active medium. However, additional techniques are needed (see [10] for a detailed summary):

- Mode-Locking: In mode-locking a phase relation between the modes in a laser resonator is achieved. This can be done by periodic modulation of the losses in the resonator, e.g. with a Kerr lens [11]. Mode-locking already leads to very short pulse trains between $3fs$ and $30ps$ [12].
- Chirped Pulse Amplification (CPA): The principle of CPA is to intentionally chirp and therefore broaden a pulse, amplify the stretched pulse and then recompress

it [13]. This is done, because the stretched pulse has a lower peak intensity and thus, has less nonlinear pulse distortion. This way, mJ-fs-pulses can be generated.

- Spectral broadening: A mJ-pulse can be broadened spectrally by coupling it into a hollow cylindrical fiber made of fused silica and filled with noble gases at high pressure. This was proposed by De Silvestri et al. [14].

- Pulse Compression: Due to the group velocity dispersion

$$GVD = \frac{d}{d\omega}\left(\frac{1}{v_g}\right) = \frac{d^2k}{d\omega^2} \tag{2.2}$$

the group velocity v_g of a pulse's spectral components is frequency-dependent. This leads in general to a situation where components with lower/higher frequency precede components with higher/lower frequency, which leads to a so called positive/negative chirp. In order to shorten the pulse duration those spectral components need to be compressed temporally, which can be done by chirped mirrors, which are mirrors made of multiple dielectric layers where several spectral components penetrate different deeply into.

2.1.2 HHG: Generation of ultrashort XUV pulses

When a femtosecond intense laser pulse with frequency ω_0 is focused into a noble gas target, such as Neon or Argon, radiation with higher harmonic frequencies $(2n+1)\omega_0$ is generated [15]. The spectral features of such radiation are [16]:

- a decrease of harmonic intensity with increasing harmonic order at lower photon energies

- a regime with constant harmonic intensity at higher photon energies for a broad energy range, which is called the plateau

- a quick decrease in the harmonic intensity after a certain photon energy $\hbar\Omega_{max}$, which is called the cut-off

The spectral range of this coherent radiation includes the XUV regime, which is defined by a wavelength range from $124nm$ down to $10nm$, or by photon energies from $10eV$ up to $124eV$, respectively [17]. The underlying process is called High Harmonic Generation (HHG). It is due to the highly nonlinear, non-perturbative interaction between electrons, initially bound to noble gas atoms, and an ultrashort intense laser pulse. The fact that radiation up to the sudden cut-off $\hbar\Omega_{max}$ can be generated within HHG, can be well described with a semiclassical three-step-model [18, 19]:

- Using the Single Active Electron Approximation and the adiabatic approximation, an electron exits the atom by tunnel ionization. Since the tunneling probability w_{tunnel} behaves like

$$w_{tunnel} \propto \exp^{-kL}, \tag{2.3}$$

where k is some constant and L the length of the tunnel, the whole interaction is nonlinear.

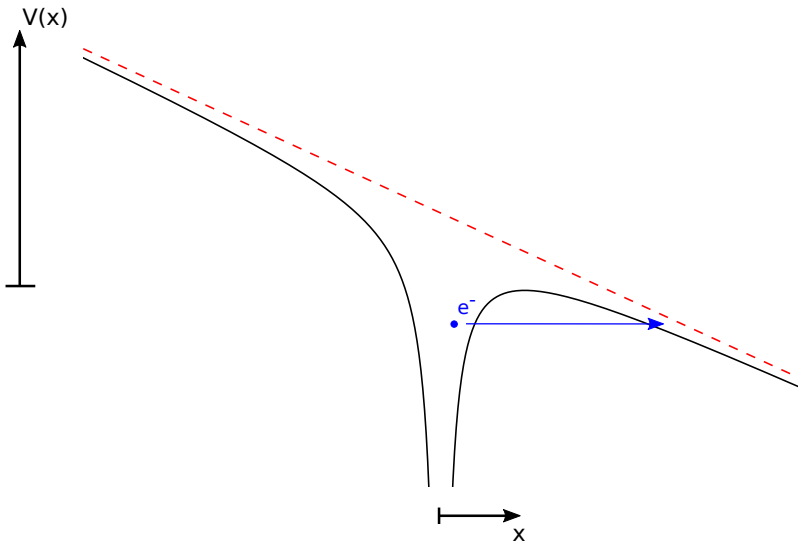

Figure 2.1: One dimensional illustration: An electron is emitted by tunnel ionization. Black: Full potential energy $V(x)$ of the electron, Red Dashed: Potential energy of the electron due to the electric field of the pulse.

- Neglecting the Coulomb field of the parent ion after ionization, the emitted electron is accelerated by the electric field of the laser pulse $E_L(t)$ (Strong Field Approximation).
- Upon reversal of the laser pulse electric field, the freed electron is accelerated back and recollision of the electron with its parent ion may happen. The excess kinetic energy plus the binding energy is emitted as a photon with high energy $\hbar\Omega$.

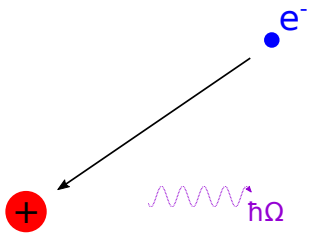

Figure 2.2: Recollision of the electron e^- with its parent ion. Generation of high-harmonic radiation $\hbar\Omega$.

Given the intensity of the initial laser pulse I_0, the ionization energy U_{ion} of an atom and the ponderomotive energy

$$U_P = \frac{I_0}{4\omega^2}, \tag{2.4}$$

which represents the quiver energy of a free electron in a harmonic electric fields, the maximal photon energy of HHG radiation was derived by [20] to be

$$\hbar\Omega_{max} = U_{ion} + 3.17U_P. \tag{2.5}$$

So far, with the three step model the presence of the plateau and the energy value of the cut-off have been explained. This shows that high-energy broadband pulses are available for spectroscopic investigations.

The mechanism described in the three-step-model takes place for every half cycle of the driving electric field, with periodicity $T/2$, being T the period of the driving electric field. According to Fourier's theorem, high harmonics with frequency spacing $2\omega_0$ can be explained.

2.2 Time-Resolved Photoelectron Spectroscopy (TRPES) of molecules

Starting with an explanation of Photoelectron Spectroscopy in ch. 2.2.1, the energy structure of molecules will be derived in ch. 2.2.2. The pump-probe technique will be introduced in ch. 2.2.3 before describing the principle of time-resolved photoelectron spectroscopy (TRPES) in ch. 2.2.

2.2.1 Photoelectron Spectroscopy (PES)

Photoelectron Spectroscopy is a quite general term and refers to all measurement techniques where observables of photoelectrons are detected. In this thesis, the observable of interest is the energy of photoelectrons. Assuming a system with discrete electronic bound states with energy $E_\alpha < 0$, the distribution of these states can be measured. This is done by exciting the system with a photon of energy hf, where the condition

$$hf > |E_\alpha| \tag{2.6}$$

must be fulfilled for emission of an electron in state α. Then the kinetic energy E_{kin} of the photoelectron is given by

$$E_{kin} = hf - |E_\alpha|, \tag{2.7}$$

which can be measured with a time-of-flight (TOF) spectrometer, as seen in Ch. 2.3. Additional information can be obtained by measuring the angular distribution of photoelectrons, like it is done for example in Angle-Resolved Photoemission Spectroscopy [21].

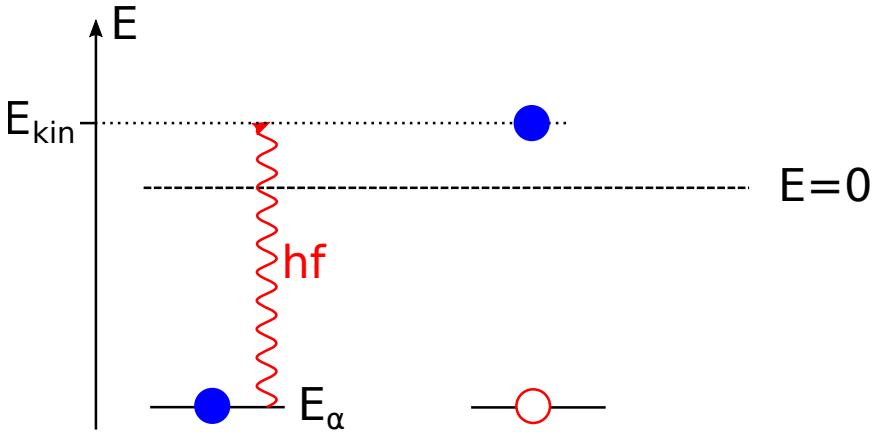

Figure 2.3: Energy diagram of photoionization with emission of an electron in state α by a photon of energy hf. The kinetic energy E_{kin} can be calculated according to Eq. 2.7.

As an example, a PES spectrum can be seen in Fig. 2.4, which was measured in our group.

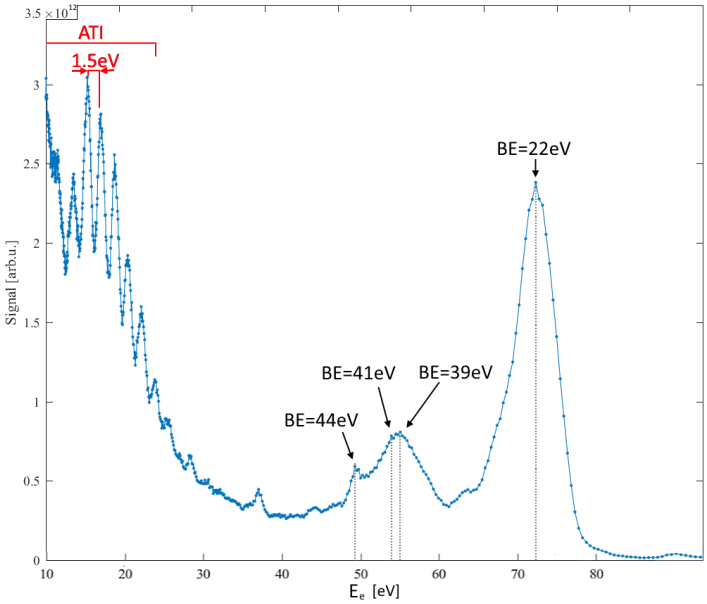

Figure 2.4: Photoelectron spectrum of SF6 ionized with IR- and XUV-pulses, with a photon energy of $1.5eV$ and $94eV$, respectively. ATI peaks below $\approx 25\ eV$ and peaks, which show the binding energies BE are marked. Figure from [22].

Photoionization can initiate a number of processes [23, p. 205], depending on whether weakly bound valence electrons or electrons from deeply bound core levels are emitted. The emission of a deeply bound electron can lead to auger-decay and shake-up processes, which also play a role in molecular ionization.

Auger decay:

In an auger decay, an electron with energy E_1 recombines with an electron hole at energy $E_0 < E_1$. The released energy $\Delta E = E_1 - E_0$ is transferred to another electron with energy E_2, which is emitted. The kinetic energy of this photoelectron is then

$$E_{kin} = \Delta E - |E_2|. \tag{2.8}$$

An illustration can be seen in Fig. 2.5.

Shake-up and Shake-off:

The sudden change of the effective charge in an atom that happens in photoionization can lead to shake-up or shake-off. Those processes have been investigated for example by T. A. Carlson and M. O. Krause [24]. Shake-up refers to the condition, when a bound electron is excited to a higher bound state, whereas shake-off describes the ionization of a bound electron, both due to the sudden change of the effective charge. As suggested

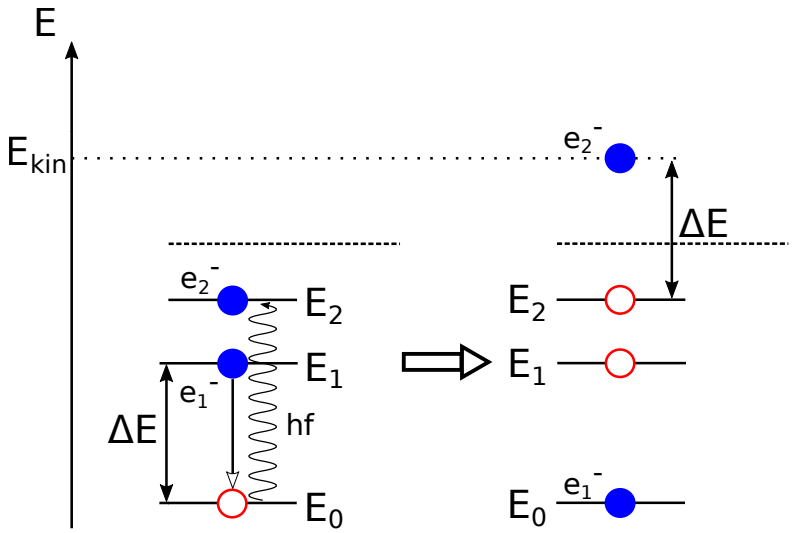

Figure 2.5: Auger decay: An electron e_1^- recombines with an electron hole with energy E_0. The released energy is transferred with a photon hf to another electron e_2^- of energy E_2, which is emitted to a free state with energy E_{kin}.

by A. Migdal [25], an electron initially in state ψ_i may transit to another state ψ'_f with a probability P_{fi} of

$$P_{fi} = |\langle \psi'_f | \psi_i \rangle|^2, \tag{2.9}$$

where the new state ψ'_f doesn't have to be a state of lower energy (shake-up). The probability $\mathcal{P}_{nl}$ for shake-off, i.e. that an electron from state nl is emitted, is

$$\mathcal{P}_{nl} = 1 - \sum_f P_{fi}, \tag{2.10}$$

where the sum goes over all bound states of the excited system.

Since the bound electrons can end up in states of higher energy and due to energy conservation, the initially emitted photoelectron has finally a kinetic energy E_{kin} lower than given by Eq. 2.7. A depiction of shake-up and shake-off can be seen in Fig. 2.6.

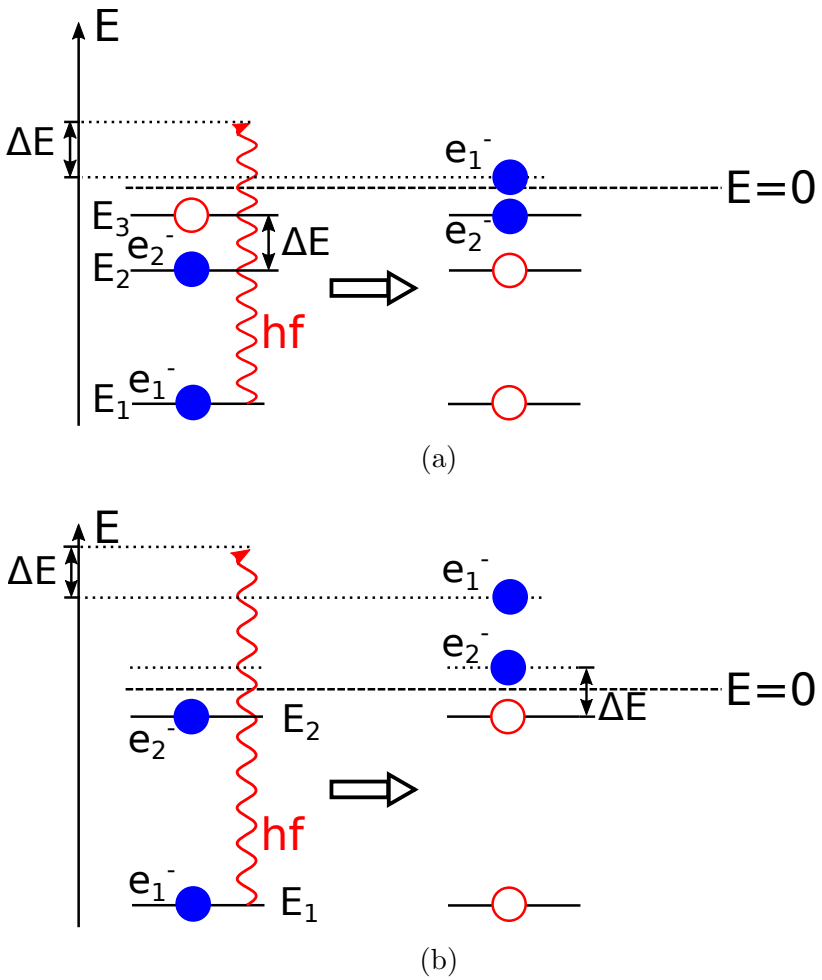

Figure 2.6: (a) Shake-up: Upon excitation with a photon of energy hf, electron e_1^- is emitted and electron e_2^- is transferred to an excited bound state E_3. (b) Shake-off: The same situation, with the difference that electron e_2^- transits to a free state.

2.2.2 The energy structure of molecules

In the following, the energy structure of molecules will be explained together with an overview of the formal derivation of B. H. Bransden and C. J. Joachain [26, ch. 9].

Given a molecule with N atoms and n electrons, the time-independent Schrödinger equation is given by

$$H_{mol}\Psi(\vec{R}_1,...,\vec{R}_{N-1},\vec{r}_1,...,\vec{r}_n) = E\Psi(\vec{R}_1,...,\vec{R}_{N-1},\vec{r}_1,...,\vec{r}_n) \tag{2.11}$$

using a coordinate system with the center of mass as origin, which reduces the number of nuclear coordinates $\vec{R}_i$ to $N-1$. H_{mol} is the Hamilton operator of the molecule, $\vec{r}_i$ are the electronic coordinates and E the energy. The Hamilton operator of the molecule

$$H_{mol} = T_{core} + T_{el} + V(\vec{R}_1,...,\vec{R}_{N-1},\vec{r}_1,...,\vec{r}_n) \tag{2.12a}$$

$$\begin{aligned} V(\vec{R}_1,...,\vec{R}_{N-1},\vec{r}_1,...,\vec{r}_n) = {} & \frac{1}{2}\sum_{\substack{i,j=1\\ i\neq j}}^{N-1}\frac{e^2}{4\pi\epsilon_0|\vec{R}_i-\vec{R}_j|} + \frac{1}{2}\sum_{\substack{i,j=1\\ i\neq j}}^{n}\frac{e^2}{4\pi\epsilon_0|\vec{r}_i-\vec{r}_j|} \\ & - \sum_{i}^{N-1}\sum_{j}^{n}\frac{e^2}{4\pi\epsilon_0|\vec{R}_i-\vec{r}_j|} \end{aligned} \tag{2.12b}$$

consists of the kinetic energy operator of the nuclei T_{core}, the kinetic energy operator of the electrons T_{el} and the potential $V(\vec{R}_1,...,\vec{R}_{N-1},\vec{r}_1,...,\vec{r}_n)$ energy, which describes the Coulomb repulsion between the nuclei and between the electrons and the Coulomb attraction between electrons and nuclei.

For an excited molecule the Hamilton operator H_{mol} is in general explicitly time-dependent. An approximation for adiabatic processes, which means that the temporal variation of H_{mol} is small on electronic time scales, is the Born-Oppenheimer approximation. In this approximation the motion of electrons and nuclei are decoupled. This is due to the fact that electrons have a much smaller mass than the nuclei, which leads to the situation that the electrons move on a much smaller time scale and the nuclei can be seen fixed regarding the electronic motion. Therefore, one can separate the Schrödinger equation into an electronic and nuclear equation and solve the former, where the kinetic energy operator of the nuclei T_{core} is omitted

$$(T_{el}+V)\phi_\alpha(\vec{R}_1,...,\vec{R}_{N-1};\vec{r}_1,...,\vec{r}_n) = E_\alpha(\vec{R}_1,...,\vec{R}_{N-1})\phi_\alpha(\vec{R}_1,...,\vec{R}_{N-1};\vec{r}_1,...,\vec{r}_n), \tag{2.13}$$

with $\phi_\alpha(\vec{R}_1,...,\vec{R}_{N-1};\vec{r}_1,...,\vec{r}_n)$ being the electronic wavefunctions, which are a function of the electronic coordinates $\vec{r}_i$ and depend parametrically on the nuclear coordinates $\vec{R}_i$. α represents the index for the electronic state. Note, that the electronic energy E_α is now a function of the nuclear coordinates $\{\vec{R}_1,...,\vec{R}_{N-1}\}$ and the potential energy surface of state α is given by

$$E_\alpha(\vec{R}_1,...,\vec{R}_{N-1}) = const. \tag{2.14}$$

The wave function for the molecule $\Psi(\vec{R}_1, ..., \vec{R}_{N-1}, \vec{r}_1, ..., \vec{r}_n)$ can be shown [26, ch. 9.1, p. 388] to be:

$$\Psi(\vec{R}_1, ..., \vec{R}_{N-1}, \vec{r}_1, ..., \vec{r}_n) = \sum_\alpha \psi_\alpha(\vec{R}_1, ..., \vec{R}_{N-1}) \phi_\alpha(\vec{R}_1, ..., \vec{R}_{N-1}; \vec{r}_1, ..., \vec{r}_n), \tag{2.15}$$

where the coefficients $\psi_\alpha(\vec{R}_1, ..., \vec{R}_{N-1})$ of the linear combination are the nuclear wavefunctions. The nuclear wavefunctions $\psi_\alpha(\vec{R}_1, ..., \vec{R}_{N-1})$ fulfill a nuclear wave equation, which is independent of the electronic wavefunctions $\phi_\alpha(\vec{R}_1, ..., \vec{R}_{N-1}; \vec{r}_1, ..., \vec{r}_n)$ in the Born-Oppenheimer approximation. In this nuclear wave equation, the nuclei move within the potential $E_\alpha(\vec{R}_1, ..., \vec{R}_{N-1})$. When solving this equation, the rotational and vibrational motion of the nuclei can be separated, giving overall three contributions to the total molecular energy $E_{\alpha,r,\nu}$: the electronic energy E_α, the rotational energy of the nuclei E_r and the vibrational energy of the nuclei E_ν:

$$E_{\alpha,r,\nu} = E_\alpha + E_r + E_\nu, \tag{2.16}$$

which depend on quantum numbers α, r and ν.

For further explanation, the energy structure of a diatomic molecule close to a minimum R_0 is shown in Fig. 2.7.

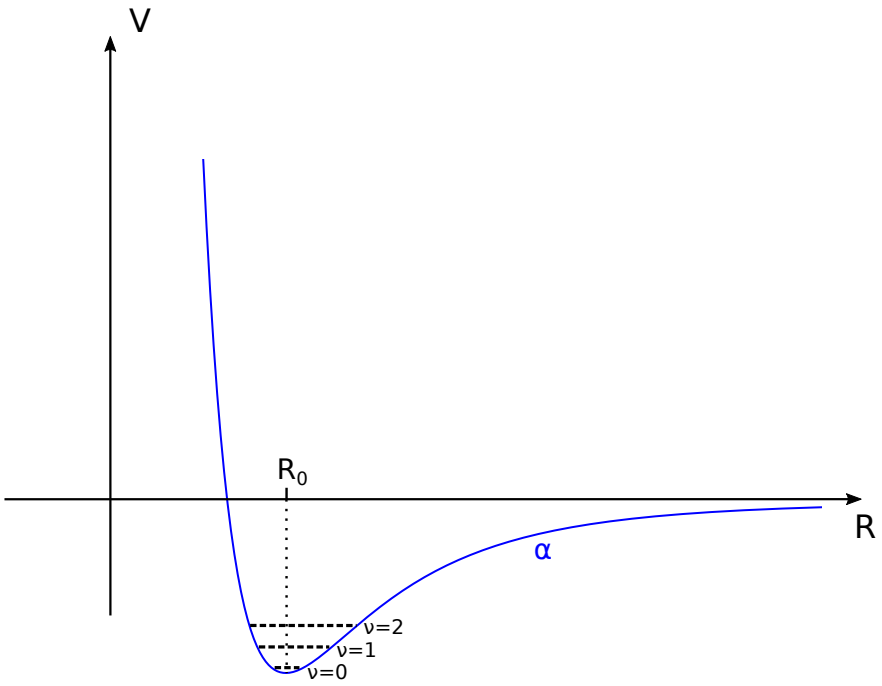

Figure 2.7: Energy structure of a diatomic molecule close to a minimum at R_0. Blue: Nuclear potential energy in electronic state α. Black dashed: Vibrational energy levels E_ν.

Here, the nuclear wave equation leads to a radial equation, which is identical to the equation for a one dimensional system with a particle with potential energy $V(R) = E_\alpha(R)$. The one dimensional nuclear motion can be approximately modelled as a quantum mechanical harmonic oscillator close to equilibrium position R_0. In this approximation the vibrational energy levels E_ν are given by

$$E_\nu = hf_0(\nu + \frac{1}{2}) \tag{2.17}$$

with h being Planck's constant and f_0 being the fundamental vibrational frequency.

2.2.3 The pump-probe technique

The principle of the pump-probe technique is to initiate a process with a pump pulse and to investigate this process with a second probe pulse. Probing for a sequence of time delays allows to reproduce the time-resolved evolution of the process under investigation. Actually, pump-probe spectroscopy is quite old: It was already realized by August Toepler, who developed the schlieren method in the period 1859-1864 [27]. Motivated by resolving density inhomogeneities in optical glasses, called 'schlieren', he investigated the propagation of sound waves which were induced by a pump spark and probed with an electronic time-delayed probe spark. The temporal resolution was limited to an order of microseconds, though the principle of the pump-prope technique is still fundamental for recent spectroscopy. Nowadays, pump-probe measurements can be performed with ultrashort laser pulses [23]. As an example, an XUV pulse $E_{XUV}(t)$ serves as a pump at time t_0 and an ultrashort IR/VIS pulse E_{IR}, delayed by some time τ, takes over the role as a probe, see Fig. 2.8. Where the reference time t_0 and the probe time $t_0 + \tau$ are defined with an uncertainty, which is proportional to the cross-correlation of the pulses. Depending on the time delay τ between the two pulses, different processes can be triggered. The XUV probe pulse could excite the system under investigation into some excited state, whereas the probe pulse induces photoionization, which leads to delay τ dependent ionization spectra in TRPES (See ch. 2.2). However, note that both, an XUV pulse and an IR pulse, can serve as a pump or as a probe, depending on the specific system under investigation.

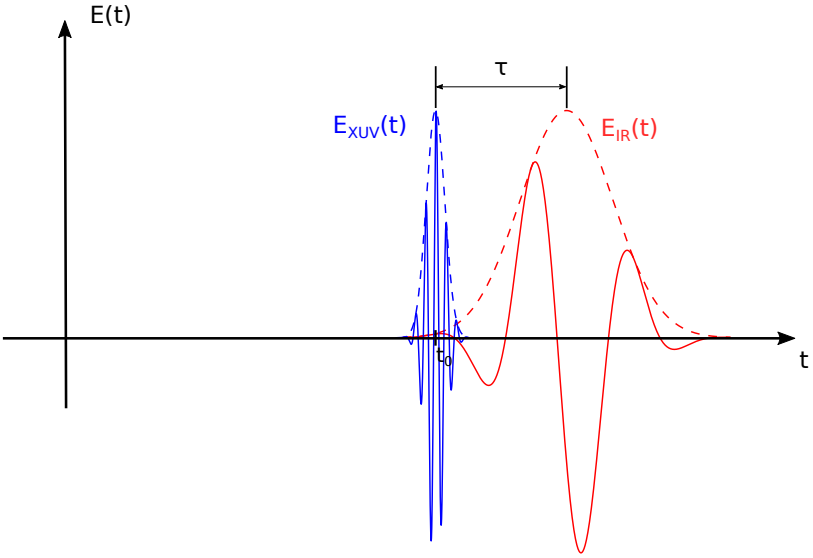

Figure 2.8: Principle of XUV-IR pump-probe measurements. An XUV pulse $E_{XUV}(t)$ serves as a pump at time t_0 and an ultrashort IR/VIS pulse E_{IR}, delayed by τ, takes over the role as a probe.

2.2.4 Principle of TRPES

The explanations in this section are oriented along a review about TRPES spectroscopy [28]. The principle of TRPES is depicted in Fig. 2.9.

First, a wavepacket $\Psi(t)$ is formed by the pump pulse

$$\Psi(t) = \sum_i c_{\alpha,\nu_i}\psi_{\alpha,\nu_i}e^{-\frac{iE_{\alpha,\nu_i}t}{\hbar}}, \quad c_{\alpha,\nu_i} \in \mathbb{C}, \tag{2.18}$$

which consists of a coherent superposition of states ψ_{α,ν_i} with energies E_{α,ν_i} and with electronic quantum number α. This wavepacket can evolve in time for the time delay τ, until the probe pulse emits an electron and puts the molecule into an ionic state α^+. Within the dipole approximation the dipole transition moment

$$d_{fi} = \langle\psi_{\alpha^+,f}(t), \phi_k|\vec{\mu}\cdot\vec{E}_{probe}|\Psi(t = t_0 + \tau)\rangle \tag{2.19}$$

describes the projection of the initial wavepacket $\Psi(t = t_0 + \tau)$ at the time $t = t_0 + \tau$ of ionization onto eigenstates consisting of ψ_{α^+,ν_i}, describing the molecular ion, and of ϕ_k, describing the photoelectron. $\vec{E}_{probe}$ describes the electric field of the probe pulse. By measuring the energy distribution of photoelectrons the relative occupation of the states ψ_{α^+,ν_i} can be determined. This can be done, because the photon energy hf_{probe} of the probe pulse is divided into the kinetic energy E_{kin} of the photoelectron and into the vibrational energy E_{α^+,ν_i} of the molecular ion. Additionally, by varying τ, information about the dynamics of the wavepacket $\Psi(t)$ can be retrieved under restriction of the pulse width Δt.

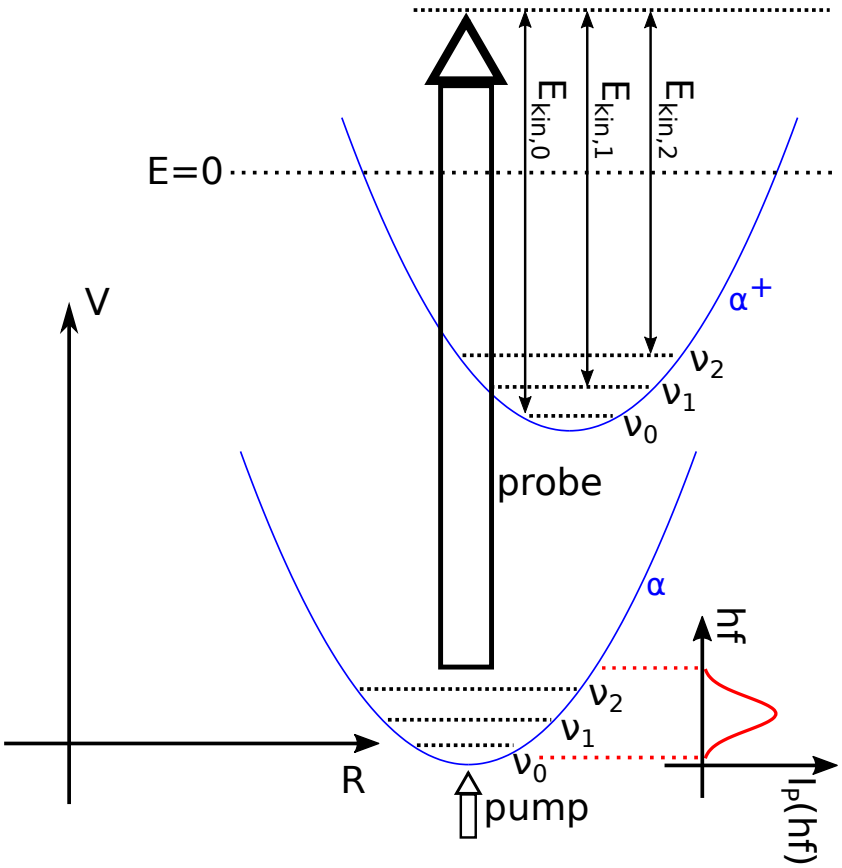

Figure 2.9: Principle of TRPES. The pump pulse, with intensity $I_P(hf)$, excites a coherent wavepacket in state α. The wavepacket can evolve for a time τ until the probe pulse ionizes the molecule, which changes to state α^+. The photon energy hf_{probe} is divided into the kinetic energy E_{kin} of the photoelectron and into the vibrational energy of the molecular ion. Figure adapted from [28, Fig. 1(a)].

2.3 Photoelectron-Photoion Coincidence (PEPICO) Spectroscopy of molecules with a single time-of-flight (TOF) spectrometer

In PEPICO the energy of photoelectrons and the type of ionic fragments are measured in coincidence. There are several ways to perform PEPICO measurements and usually two TOF spectrometers are used [29, p. 295-298]. In the following, a measurement method is described, for which a single TOF spectrometer is sufficient.

2.3.1 Performing PEPICO measurements with a single TOF spectrometer

The measurement principle of PEPICO with a single TOF spectrometer can be seen in Fig. 2.10.

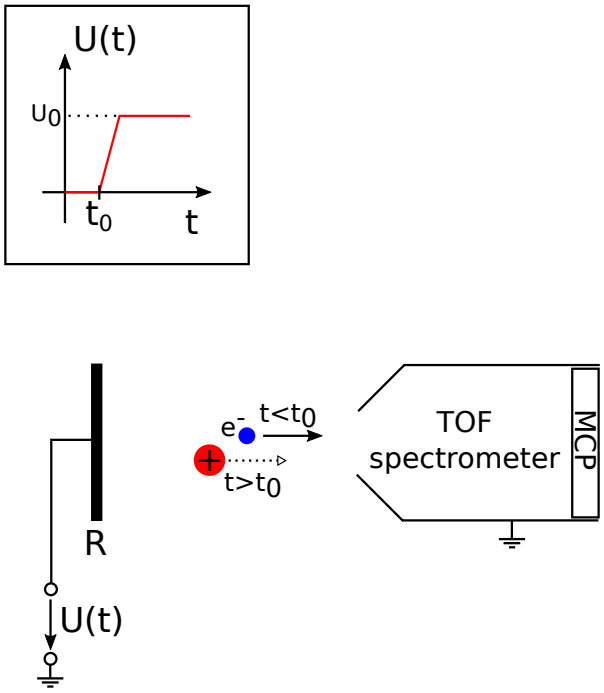

Figure 2.10: Illustration of a PEPICO measurement setup with a TOF spectrometer.

After an ionization event, the energies of photoelectrons are detected by measuring their time-of-flight $t_{el,TOF}$ in a TOF spectrometer. For this, the electrons are guided by electrostatic lenses towards a Microchannel Plate detector (MCP). Then, at time t_0, an external voltage U_0 is applied to a repeller with a rise time much smaller than the time-of-flight $t_{ion,TOF}$ of the ionic fragments, while the TOF spectrometer stays on ground. The external voltage U_0 drives the molecular ions into the direction of the TOF entrance in order to measure their time-of-flight $t_{ion,TOF}$. By measuring the ionic time-of-flight

$t_{ion,TOF}$, the ratio between electric charge and mass q/m of the molecular ions can be calculated, which enables to determine the species of ion.

2.3.2 Benefits of PEPICO

When a molecule is ionized, it can end up either in a bonding, or in an antibonding state, see Fig. 2.11. Molecular fragmentation can happen in the former case in a highly vibronic state, or in the latter case. The whole energy structure of a molecule consists of several potential energy curves, that allow a vast number of final states, even for the simplest molecules [30]. All those final states contribute to the photoelectron spectrum, making those spectra very complex and the retrieval of the full molecular dynamics difficult. This level of complexity can be drastically reduced by PEPICO, which means detecting for every photoelectron the corresponding ionic fragment, i.e. measuring photoelectrons and ions in coincidence. This makes it possible to separate the whole photoelectron spectrum of the molecule into the photoelectron spectra of the individual ionic fragments. In Fig. 2.12, an illustration of PEPICO for an ionization event with two possible antibonding final states is shown.

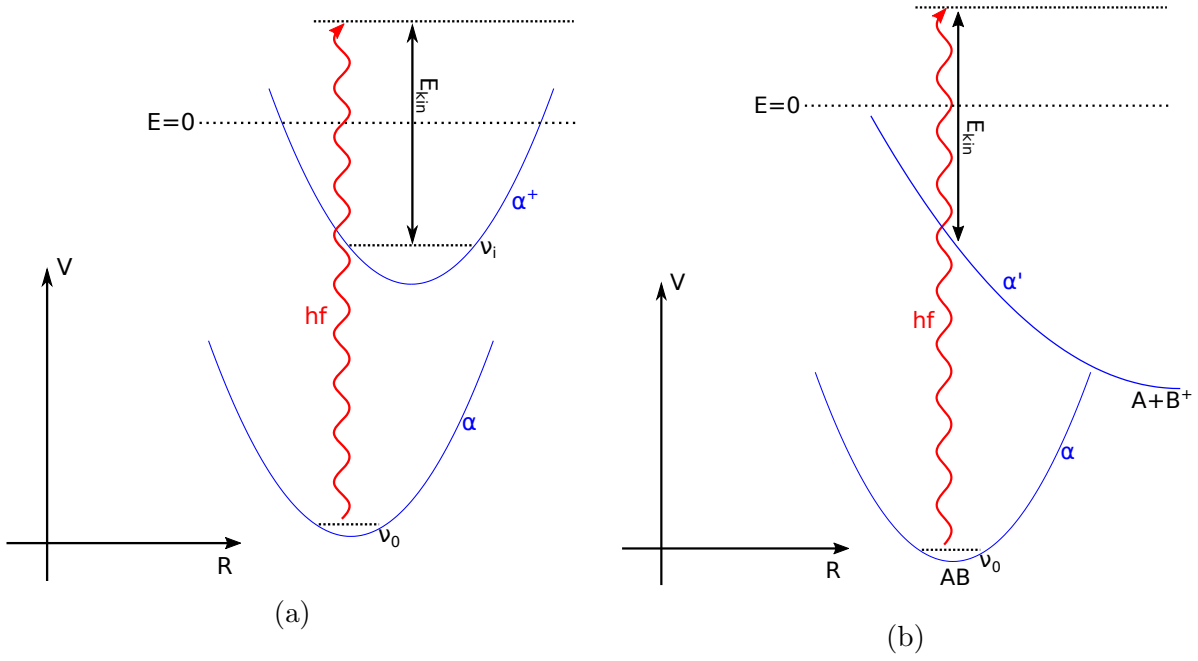

Figure 2.11: (a) Photoionization of a molecule, initially in state Ψ_{α,ν_0}, by a photon with energy hf to an ionized bonding state Ψ_{α^+,ν_i}. The photoelectron has kinetic energy E_{kin}. (b) Photoionization of a molecule AB, initially in state Ψ_{α,ν_i}, by a photon with energy hf to an electronic antibonding state $\Psi_{\alpha'}$, in which the molecule AB separates into fragments A and B^+.

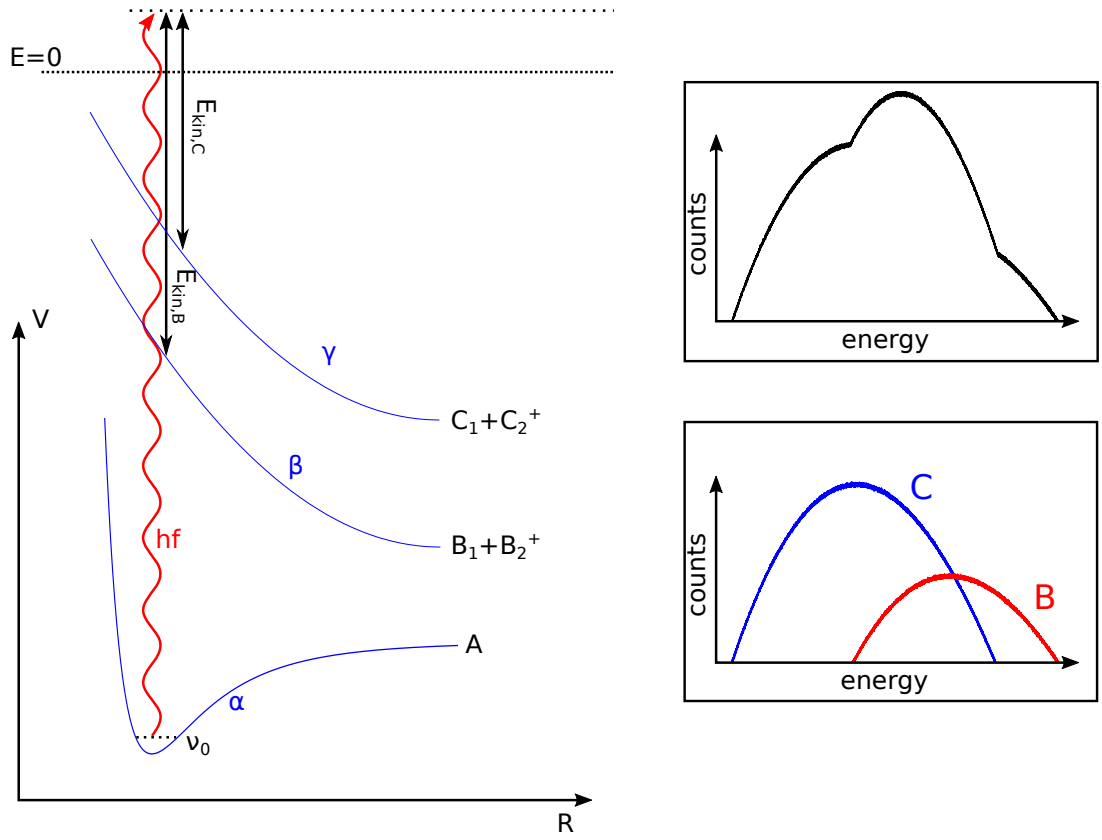

Figure 2.12: Left: Photoionization of a molecule, initially in state Ψ_{α,ν_0}, by a photon with energy hf. There are two possible antibonding final states Ψ_β and Ψ_γ, in which the molecule separates into two fragments with one ionized each. Right: Full photoelectron spectrum of the ionization event (black). Photoelectron spectra of the fragments, which can be measured with PEPICO (red, blue).

3 Experimental setup

The PEPICO measurements, which are carried out in scope of this work, are performed with ultrashort laser pulses in an experimental chamber, equipped with a single time-of-flight (TOF) spectrometer. A detailed description of the XUV beamline and the experimental chamber can be found in [22].

Ultrashort IR pulses are generated by a Kerr-lens mode-locked Ti-Sapphire laser, whose initial pulses ($\approx 6fs$ pulsewidth, $4.5nJ$ pulse energy, $80MHz$ repetition rate), are amplified by a chirped pulse amplifier, which is pumped by a diode pumped Nd:YAG laser. Pulses are selected with a Pockels cell with a repetition rate of $5kHz$. The pulse energy after amplification is around $800\mu J$. The pulses are spectrally broadened after amplification by coupling them into a hollow cylindrical fiber filled with Neon with a core diameter of $250\mu m$ and then recompressed by chirped mirrors to a sub-10fs pulsewidth. The beamline is also capable of generating XUV pulses, by focussing the IR pulses thereupon into an XUV target gas. In order to show the possibility of PEPICO measurements with the nanosecond high-voltage electrical switch in this XUV beamline, measurements were performed with IR pulses, due to the higher ionization yield.

The experimental setup in the experimental chamber is shown in Fig. 3.1. The pulses enter the chamber at the entrance E. The focus of the pump-IR and probe-IR pulse on the gas target G and their delay in the focus are set by a split mirror M, whose central part could be shifted by a closed-loop piezo stage $TS2$. By illuminating the central and annular part of the mirror, two reflections time delayed to each other are obtained. The position of the gas target G can be set by a translational stage $TS1$. The repeller plate P can be seen right in front of the time-of-flight spectrometer TOF. The high-voltage electrical switch is placed right on top of the chamber. The high voltage on the output of the switch is provided over an RG58 coaxial cable, which is connected with an SHV connector built into the chamber wall at C with a solder termination inside the chamber. A copper wire W is soldered on this solder termination on one end and screwed on the plate on the other end. Together, the copper wire and the coaxial cable serve as transmission line for the voltage from the electrical switch to the repeller plate P (see ch. 6.1). The RC line termination is soldered on one end on the copper wire, which is screwed on the plate, and screwed on the TOF spectrometer at S on the other end. It was checked, that S is connected to ground. In the TOF spectrometer (see Fig. 3.2) electrons and ions are detected with a microchannel plate detectors (MCP). The TOF spectrometer is pumped by a separate turbopump for keeping the vacuum of $\approx 10^{-7}mbar$ in the TOF spectrometer.

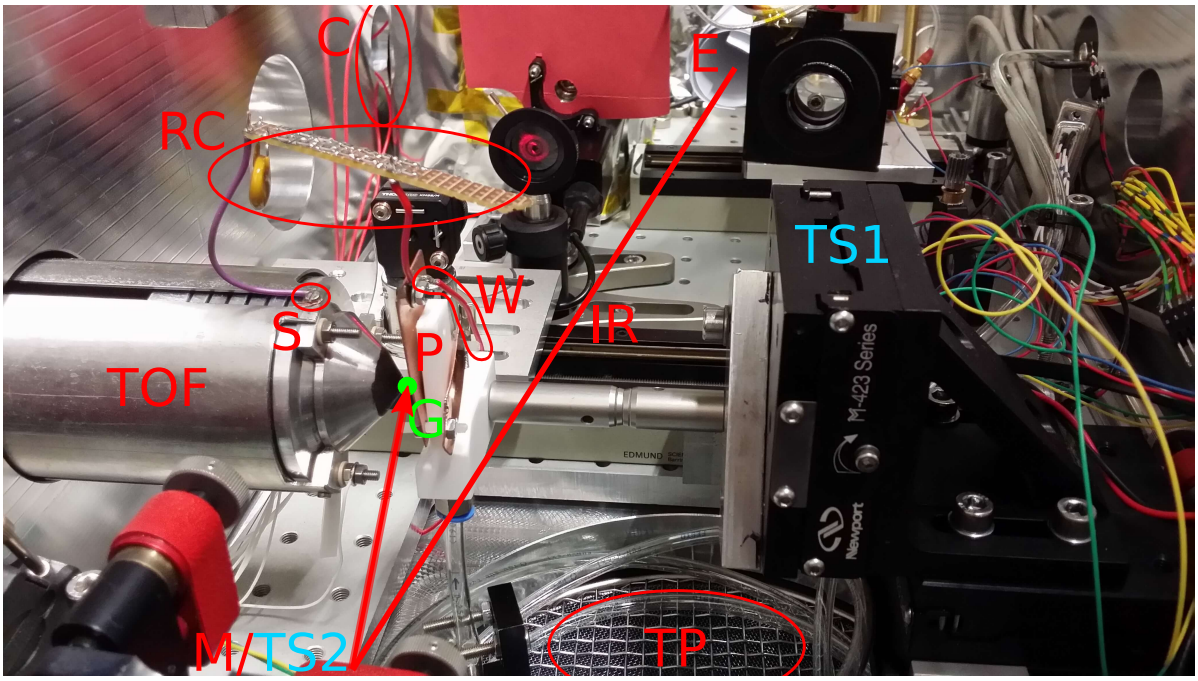

Figure 3.1: Experimental setup in the experimental chamber.

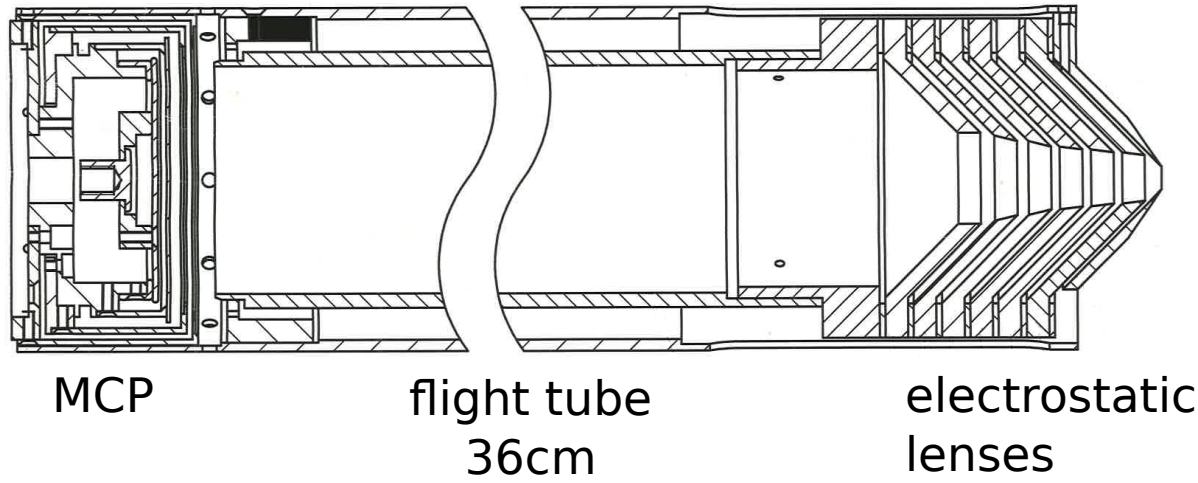

Figure 3.2: Time-of-flight spectrometer used for PEPICO measurements.

4 Nanosecond rise-time high-voltage electrical switch

In order to perform PEPICO measurements as described in ch. 2.3, a high-voltage switch with a rise time of just a few nanoseconds and a repetition rate in the order of $1kHz$ is needed. Such a switch was developed in scope of this diploma thesis and will be presented in this chapter.

4.1 Schematic overview

A schematic overview of the device can be seen in Fig. 4.1. The topology of the switch circuit was proposed by Feng et. al. [31].

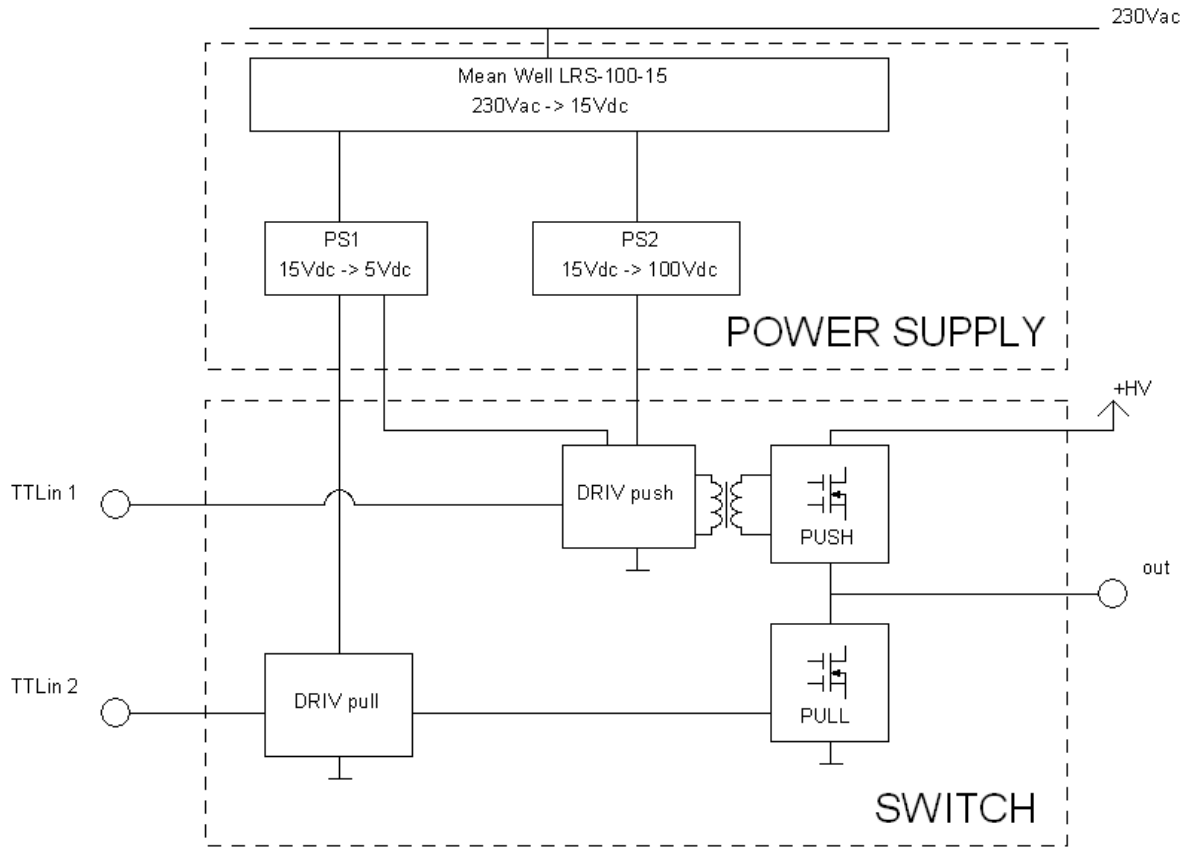

Figure 4.1: Schematic overview of the electrical switch.

The switch works in a push-pull configuration, where each side of the switch ($PUSH$ and $PULL$) consists of power MOSFETS, which are connected in series. The reason for connecting power MOSFETS in series is, that as far as known by the author, there are no power MOSFETs currently available which have both, a minimal drain-source breakdown voltage of $2kV$ and a rise time below $10ns$. Both sides are driven by driver circuits ($DRIV\ push/pull$), whose inputs accept TTL signals ($TTLin$ 1/2) [32]. The power is provided by the power line, whose AC voltage of $230Vac$ is transformed into $15Vdc$ by a switching power supply ($Mean\ Well\ LRS$-100-15), which is able to provide an output power of up to $105W$ or up to $7A$ of output current, respectively. Then, the voltage of $15Vdc$ is transformed by a buck-converter circuit $PS1$ to $5Vdc$ and by a boost-converter circuit $PS2$ to $100Vdc$ in parallel. In the following sections, every part of the whole circuit will be explained in detail. The circuit was built with discrete elements on a laboratory card ($RE200 - LF$) as can be seen in Fig. 4.2.

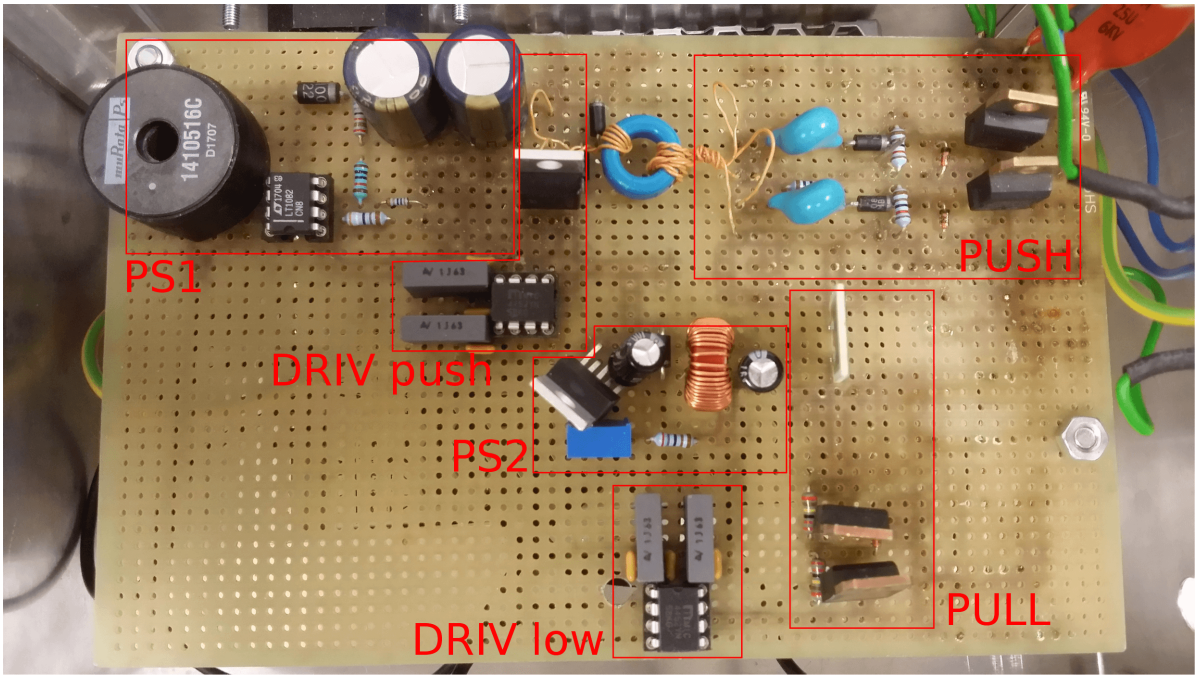

Figure 4.2: Laboratory card of the nanosecond rise-time high-voltage electrical switch.

4.2 Switch

4.2.1 Push circuit

Fig. 4.3 shows the schematic of the push circuit, which drives the output from $0V$ to U_{HV}.

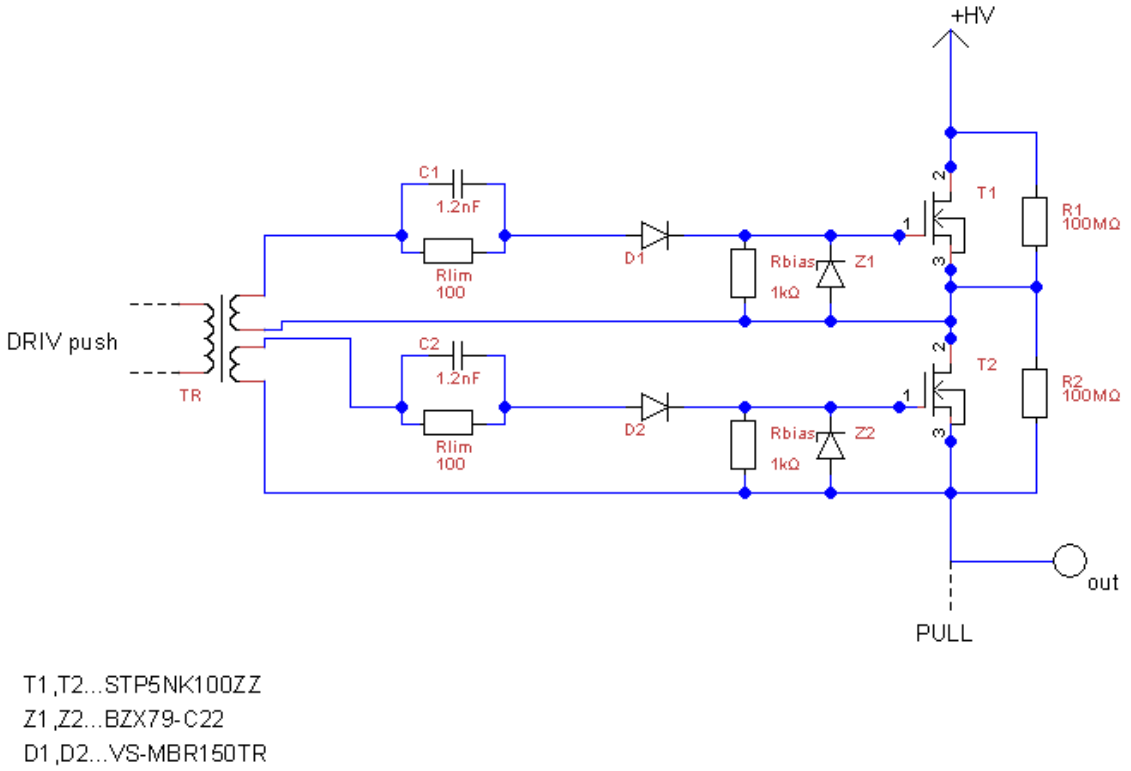

Figure 4.3: Schematic of the high-side circuit.

The circuit is driven inductively over a transformer TR with a toroidal ferrite core ($EPCOS\ N30$) and two secondary windings. The primary and secondary windings are trifilar wound with 5 turns each. This leads to symmetric voltage pulses on the secondary sides, which is important, such that both MOSFETs $T1/T2$ switch at the same time and provide a rising edge with a constant slope when turning on. The capacitor $C1/C2$ provides a low impedance for the gate driving pulse, while the resistor R_{lim} limits the gate current. The diode $D1/D2$ prevents unwanted discharge of the gate-source capacitance of $T1/T2$. The gate-source capacitance is discharged over resistor R_{bias}. By changing R_{bias} the on-time of the high side can be changed. The Zener diode $Z1/Z2$ clamps the gate-source voltages of $T1/T2$ to prevent damage. The resistors $R1$ and $R2$ provide an equal voltage sharing between the transistors $T1$ and $T2$.

4.2.2 Pull circuit

The schematic of the pull circuit can be seen in Fig. 4.4. When the output is on U_{HV}, triggering the pull circuit will set the output to $0V$.

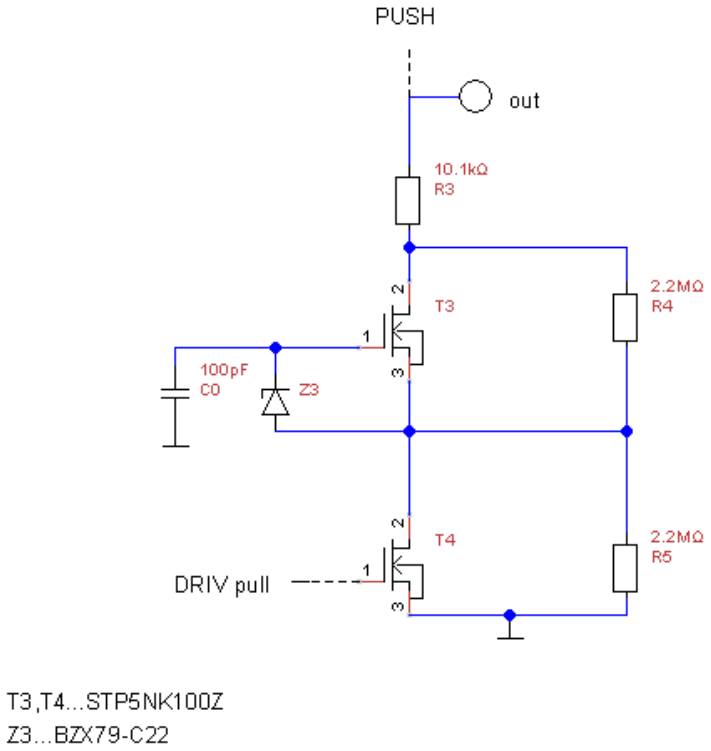

Figure 4.4: Schematic of the pull circuit.

When the output is on high voltage U_{HV}, the capacitor C_0 is charged on voltage $\approx U_{HV}/2$ within a time dictated by $(R3 + R4)C0 \approx 220\mu s$. When the driver *DRIV pull* charges the gate-source capacitance of transistor $T4$, the drain voltage of $T4$ goes to ground. This raises the gate-source voltage of transistor $T3$ maximally to the zener voltage, clamped by zener diode $Z3$, because of discharge of capacitor $C0$ over the zener diode. With this way, $T3$ also turns on quickly, which leads to a discharge of the output over resistor $R3$ and the transistors $T3$ and $T4$. The resistors $R4$ and $R5$ are for voltage sharing between transistors $T3$ and $T4$, and for providing a current path in order to charge capacitor $C0$, when the output is on U_{HV}.

During operation of the switch at a repetition period of $600\mu s$ it has been noticed, that the transistor $T3$ is not triggered, until the output voltage is above $\approx 400V$ and that the fall time of the output voltage from high voltage to ground becomes less the higher the output voltage (see ch. 6.1.3). In order to prevent a long fall time at low voltages a zener diode with a lower zener voltage, but still above the gate-source threshold voltage of transistor $T3$, is advised.

4.2.3 Driver circuits

The driver circuit *DRIV push* is shown in Fig. 4.5.

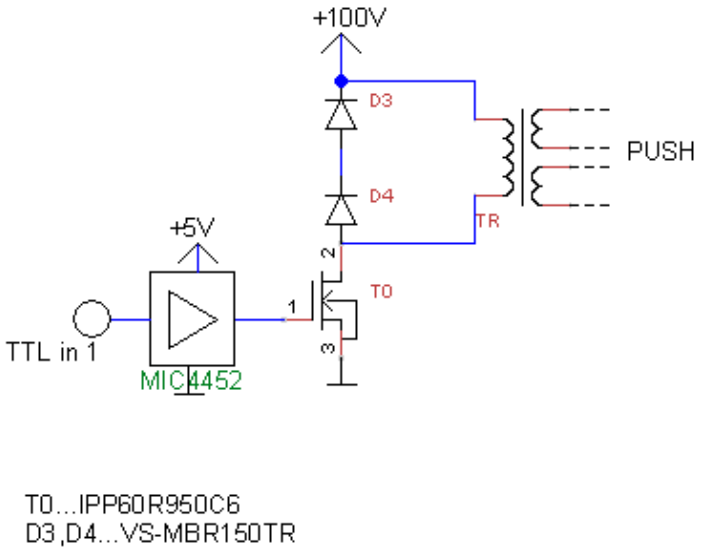

Figure 4.5: Schematic of the driver circuit *DRIV push*.

*MIC*4452 is a very fast MOSFET driver, which quickly charges the gate-source capacitance of transistor T_0 on $+5V$, which then pulls its drain to ground. This way, $+100V$ is applied to the primary side of the transformer TR, which leads to a current pulse. Because of the relationship

$$u_{prim} = L_{equ} \frac{di_{prim}}{dt}, \tag{4.1}$$

where u_{prim} and i_{prim} are the voltage and the current of the primary side, respectively and L_{equ} is the equivalent inductivity of the transformer, the transistor $T0$ should conduct for just a very short time ($\approx 10ns$). Otherwise, the current i_{prim} would rise until the transistor $T0$ burns out. Diodes $D3$ and $D4$ prevent voltage peaks, which would otherwise happen, when $T0$ switches from 'on' to 'off'.

The driver circuit *DRIV pull* consists only of a *MIC*4452, provided with a supply voltage of $+5V$.

4.3 Power Supply

4.3.1 Switching regulators

A switching regulator is a regulated DC-to-DC converter, which has a high power efficiency. The basic elements of a switching regulator are a transistor, a coil or a transformer and a logic circuitry, which compares the output voltage with some internal reference over a feedback loop. There are various kinds of switching regulators, the most

important are the buck-converter, which lowers the input voltage, the boost-converter, which raises the input voltage and the inverting converter, which inverts the input voltage. In the following, the principles of the buck-, and the boost-converter will be explained, since they are used for the power supply of the high-voltage switch. Those explanations are oriented along an introduction to switching regulators in [33, p.641-647]. The voltages in the following schematics are in reference to ground, unless otherwise specified with an arrow.

Buck-Converter

The principle of a buck-converter is illustrated as a schematic in Fig. 4.6.

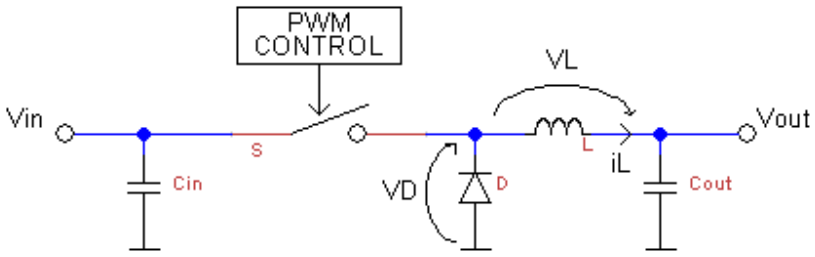

Figure 4.6: Principle of a buck-converter.

The capacitors C_{in} and C_{out} serve as bypass capacitors for reducing voltage ripples. A pulse-width-modulation (PWM) control controls the on-time t_{on} of the switch S. When the switch S is 'on', the voltage V_L applied to the coil L is $V_{in} - V_{out}$, neglecting the voltage drop over the switch S. Therefore, the current i_L through the coil is rising with a constant slope

$$\frac{di_L}{dt} = \frac{V_{in} - V_{out}}{L}. \tag{4.2}$$

When the switch is 'off', the slope of the current i_L is

$$\frac{di_L}{dt} = \frac{-V_D - V_{out}}{L}, \tag{4.3}$$

with V_D being the forward-voltage of diode D, which is now conducting. In steady-state operation, the rise of current during on-time t_{on} must be as large as the decrease of current during off-time t_{off}:

$$\frac{V_{in} - V_{out}}{L} t_{on} = \frac{V_D + V_{out}}{L} t_{off}, \tag{4.4}$$

which leads to

$$V_{out} = V_{in} \frac{t_{on}}{T} - V_D(1 - \frac{t_{on}}{T}) \approx V_{in} \frac{t_{on}}{T} = V_{in} D, \tag{4.5}$$

with T being the switching period. So the output voltage is approximately given by the input voltage V_{in} multiplied with the duty cycle D. So the PWM control can regulate the voltage over the duty cycle D. This is done by feedback of the output voltage V_{out} and by comparison with some internal reference voltage.

Boost-Converter

The principle of a boost-converter is depicted in Fig. 4.7.

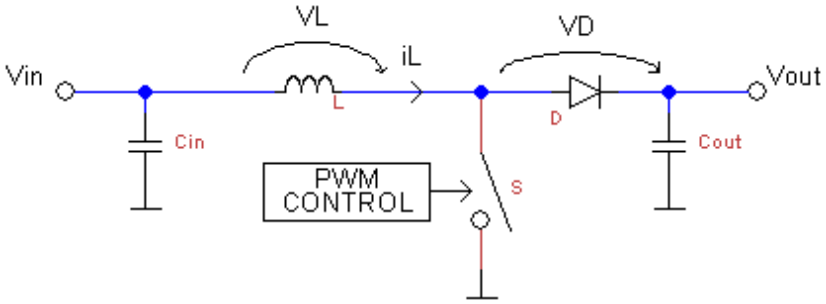

Figure 4.7: Principle of a boost-converter.

The working principle is similar to the principle of the buck-converter: A PWM control regulates the output voltage V_{out} over the duty cycle $\frac{t_{on}}{T}$. Neglecting the voltage drop over the switch S, the slope of current i_L is

$$\frac{di_L}{dt} = \begin{cases} \frac{V_{in}}{L} & ,S \text{ 'on'} \\ \frac{V_{in}-V_{out}-V_D}{L} & ,S \text{ 'off'} \end{cases} \tag{4.6}$$

For steady-state operation

$$\frac{V_{in}}{L} t_{on} = -\frac{V_{in} - V_{out} - V_D}{L} t_{off} \tag{4.7}$$

must be fulfilled, which leads to

$$V_{out} = V_{in} \frac{1}{1 - \frac{t_{on}}{T}} - V_D \approx V_{in} \frac{1}{1 - D}. \tag{4.8}$$

4.3.2 PS1

In Fig. 4.8 the buck-converter circuit PS1 can be seen. Its centerpiece is the $TI\ LM2585 - ADJ$ buck-converter. The schematic is adopted from the datasheet [34, p. 26]. The output voltage can be set with the potentiometer $\Delta R = 10\Omega...2M\Omega$ to

$$V_{out} = V_{ref}(1 + \frac{R7 + \Delta R}{R6}) \quad , V_{ref} = 1.23V. \tag{4.9}$$

This leads to $\Delta R \approx 3k\Omega$ for an output voltage of $5V$. It is recommended to fine adjust the value of ΔR regularly for best performance of the switch.

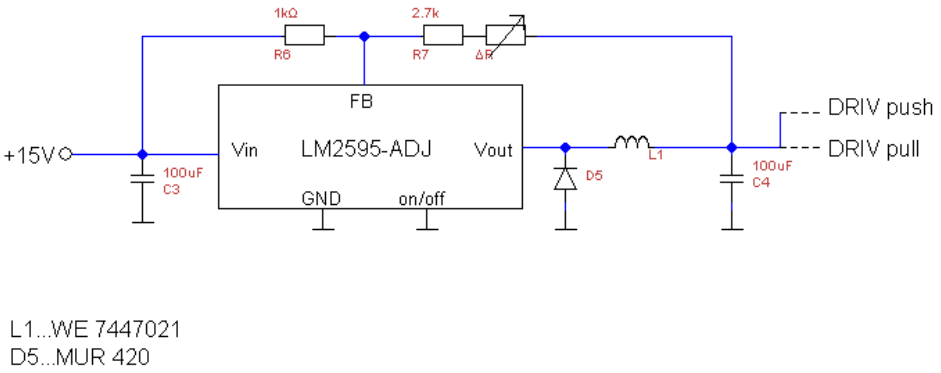

Figure 4.8: Schematic of the power supply circuit $PS1$.

4.3.3 PS2

In Fig. 4.9 the circuit of $PS2$ can be seen, where the $LT1082$ from Linear Technology works as boost-converter. The schematic is adopted from the datasheet [35, p.10].

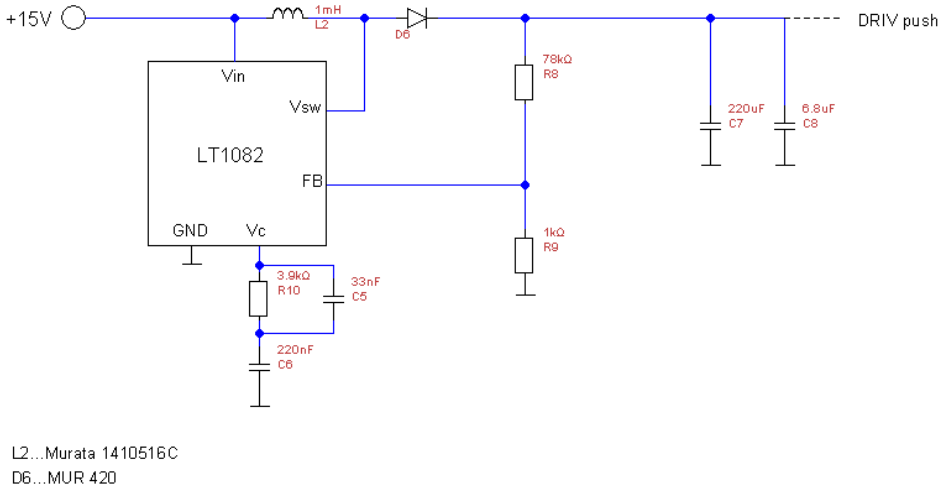

Figure 4.9: Schematic of the power supply circuit $PS2$.

According to [35], the output voltage V_{out} is given by

$$V_{out} = V_{ref}(1 + \frac{R8}{R9}) = 97.17V \quad , V_{ref} = 1.23V. \tag{4.10}$$

4.4 Chassis and connectors

Switching high voltages in nanoseconds leads to electromagnetic radiation and, due to parasitic inductivities and high peak-currents, proper grounding is important. Electromagnetic radiation is handled by putting the whole device into a chassis made of aluminium sheet, see Fig. 4.10. Additionally, the chassis can be used as grounding reference, which is connected with the ground of the power line over the main switching supply. For the individual modules of the device, star grounding points $P1$, $P2$ have been realized and it has been taken care of making the connections as short as possible. The push-circuit has been grounded separately at $S2$, since it is galvanically isolated from the driver $DRIVpull$.

For the connection to the power line a cold-device plug IEC-60320 C14 is used. The driver signals $TTLin$ 1/2 are supplied by BNC-connectors. SHV-connectors are used for high voltages.

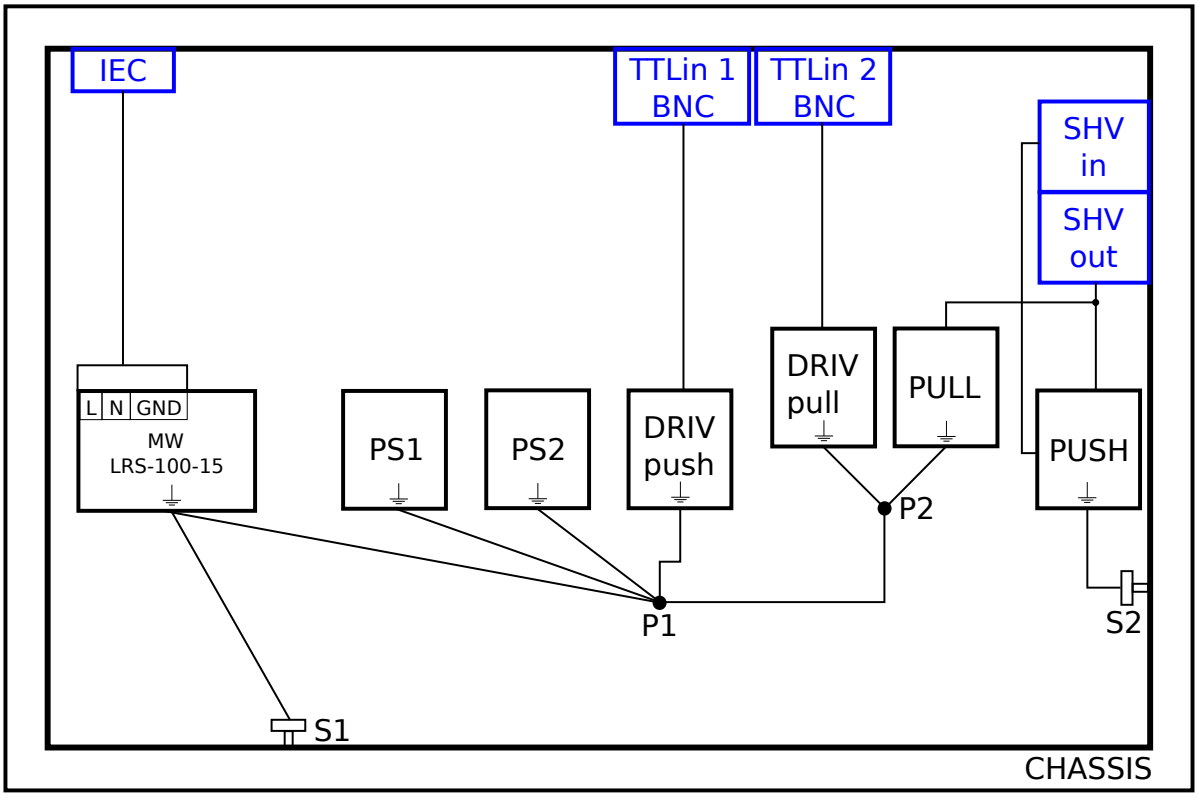

Figure 4.10: Illustration of grounding and connections. Connectors are in blue.

4.5 Way of operation

The high-voltage switch is controlled by its inputs $TTLin$ 1 and $TTLin$ 2 over a BNC connector. A pulse generator with two or more outputs can be used for controlling the switch, as it is done in ch. 6.1.

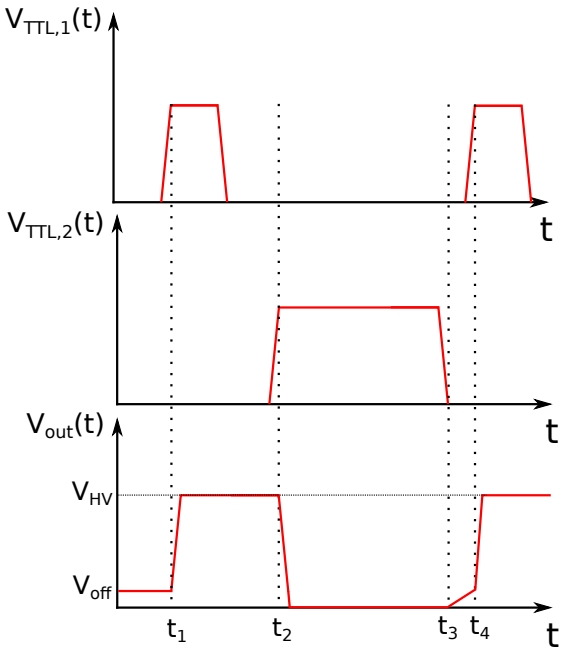

Figure 4.11: Way of operation

The way of operation is illustrated in Fig. 4.11. The figure shows the input signals $V_{TTL,1}(t), V_{TTL,2}(t)$ for the drivers of the push-, and the pull-side of the switch, respectively and the output voltage V_{out}. Before t_1 only the high voltage V_{HV} is applied, while the push-side, as well as the pull-side, is 'off'. Because of the voltage divider, made of the voltage sharing resistors $R1, R2, R4, R5$ (See Sec. 4.2.2,4.2.1), there is an offset voltage V_{off} at the output. When the push-side of the switch is triggered at t_1, the output is driven to U_{HV}. The push-side stays on, as long as the gate-source capacities of MOSFETS $T1$ and $T2$ stay above their threshold voltage $U_{th} \approx 3.75V$. This on-time can be set by the bias resistor R_{bias}. It is important, that triggering the pull-side of the switch doesn't happen before the push-side switches to 'off'. Otherwise, there would be a short-circuit of the high voltage U_{HV} to ground over the transistors $T1 - T4$. When triggering the pull-side of the switch at t_2 with the push-side on 'off', the output goes to ground and stays there as long as the pull-side is triggered until t_3. Between t_3 and t_4, after untriggering the pull-side, a recharge of the output on V_{off} happens. At any time after t_3 the push-side of the switch can be triggered again. If a turn-on delay $\Delta t = t_4 - t_3$ as small as possible is needed, a pulse generator with very low jitter and precise synchronization between $V_{TTL,1}(t)$ and $V_{TTL,2}(t)$ is necessary in order to prevent a short-circuit.

The repetition rate of the switch is limited by:

- The limited power of the high-voltage source, which provides U_{HV}. This is by far the most limiting factor, since charging the capacities of the switch (drain-source capacities of transistors, parasitic capacities in cables, capacitive loads, dedicated capacitors in the circuit) on high voltages consumes an average current, which is directly proportional to the repetition rate.
- The discharge time of transistor gates $T1$ and $T2$
- Imperfect synchronization between $TTLin$ 1 and $TTLin$ 2
- The fall-, and rise-time of the push-, and the pull-side

The rise time t_r of the high-voltage switch is mostly given by the rise time $t_{r,T}$ of the transistors $T1$ and $T2$, which is 7.7 ns according to [36] and, in case of a capacitive load C_L, by the RC time constant t_{RC} of the capacitor C_L when charging over the on-resistances of the transistors $T1$ and $T2$:

$$t_r \approx t_{r,T} + t_{RC}. \tag{4.11}$$

5 PEPICO program

The task of the PEPICO program is to process the experimental data, visualize the data during the experiment and to control the piezo element. A functional diagram for the experimental data flow and the measurement control can be seen in Fig. 5.1.

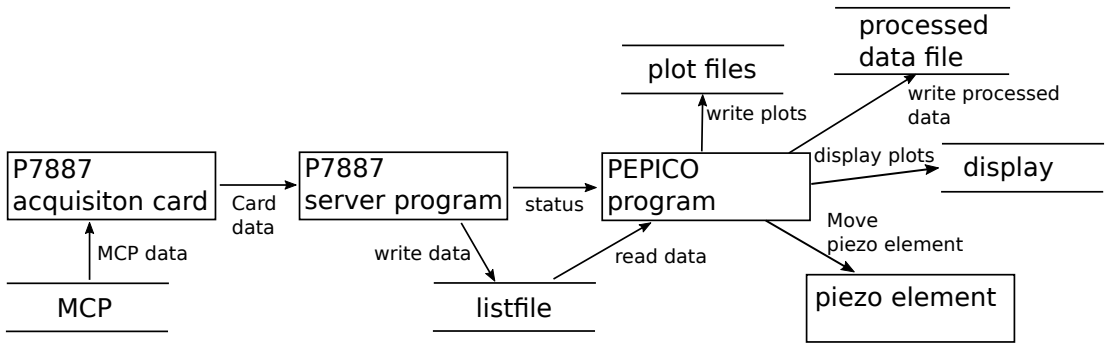

Figure 5.1: Functional diagram for the experimental data flow and the measurement control.

The data from the MCP detector is acquired by an acquisition card (*FAST ComTec P*7887) and managed by its server program. With this program, a listfile, which contains all experimental results, can be written. The PEPICO program can read the data from this listfile and it is also possible to read the status of the server program, whether a measurement is running or not. The PEPICO program is able to control the piezo element, which sets the time delay between pump- and probe-pulse, it can write processed data and plots to files and it can display the plots from a recent measurement.

The program consists of three classes, see Fig. 5.2, which are:

- Class Pepico, which is the main class and controls the whole experimental procedure over a method stepThread() and processes the data read from listfile over a method processData(). It also includes methods save() and load() for saving/loading the configurations set in the Graphical User Interface.
- Class QTableList, which handles the scan points list, see Fig. 5.4(b).
- Class Acquire: This class is the interface to the P7887 server program and imports the P7887.dll-file. Therefore, it is responsible for checking the running status (isRunning()), and controlling the acquisition (startAcquisition(), stopAcquisition(), pauseAcquisition).

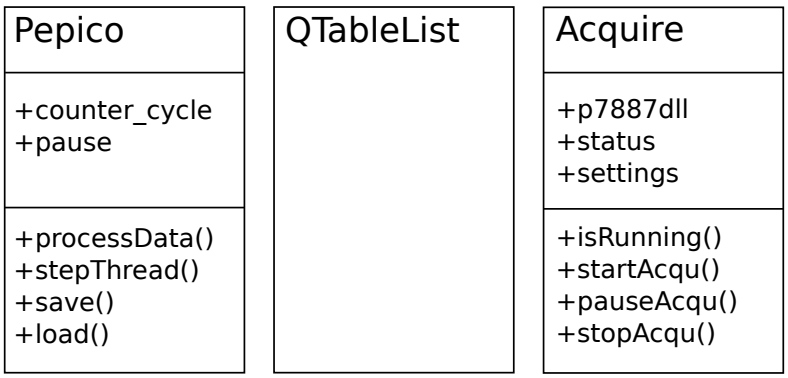

Figure 5.2: Class diagram of the PEPICO program. For the purposes of clarity, only the basic attributes and methods are given.

The program also has a module "piezojena.py", which provides methods for controlling the piezo element. Those methods are called from class Pepico.

A flowchart of methods stepThread() and processData() can be seen in Fig. 5.3. By clicking 'Run' in the GUI, stepThread() is started. The measurement can also be paused by clicking 'Pause', which stops the acquisition, but doesn't reset the counters. Also, the measurement can be resetted by clicking 'Reset', which stops the measurement and resets the counters. Both methods also check, whether the processed data or the generated plots should be saved. The user can control this by (un-)checking checkboxes 'Save plots as PDF' and 'Save processed Coinc. Data'.

The difference between the raw data from the P7887 card and the processed data is the following: In the raw data for every laser shot, there is a zero, which marks the start of the acquisition for this shot and eventually some numbers between zero and the number of maximal time bins. The latters mark detection events at the time bin with the given numbers. The processed data consists of rows, one row for every laser shot, where an event has been detected. Every row is divided into a list of electron times-of-flight and a list of ion times-of-flight, which are detected for this laser shot. So the processed data contains the measurement data as coincidences.

The whole graphical user interface (GUI) can be seen in Fig. 5.4. On the left side of the GUI the directory and the .dll-file location can be set. Also the measurement can be controlled on the left side and the steps, which were already done are displayed. In 5.4.(a) the whole GUI with tab 'Piezo control' clicked can be seen, where the piezo position, the conversion factor $fs/\mu m$ and the waiting time after moving the piezo can be set. The scan settings are shown in Fig. 5.4.(b). Here, the scan range can be set, and by clicking 'Fill', the list of scan points is shown. There are also some other settings, which can be shown by clicking the tab 'Other settings', Fig. 5.4.(c).

The Pepico program was written on the basis of the program 'Splittex', which was written by Vaclac Hanus for other measurements in our working group. The module 'piezojena.py' and the class QTableList have been taken without changes. The main class Splittex in 'Splittex' has been renamed to class Pepico in the Pepico program and major changes have been done. The methods stepThread() and processData() have been

rewritten in order to be used for PEPICO measurements and the GUI has been adapted. Class Acquire was written completely from scratch by the author of this thesis.

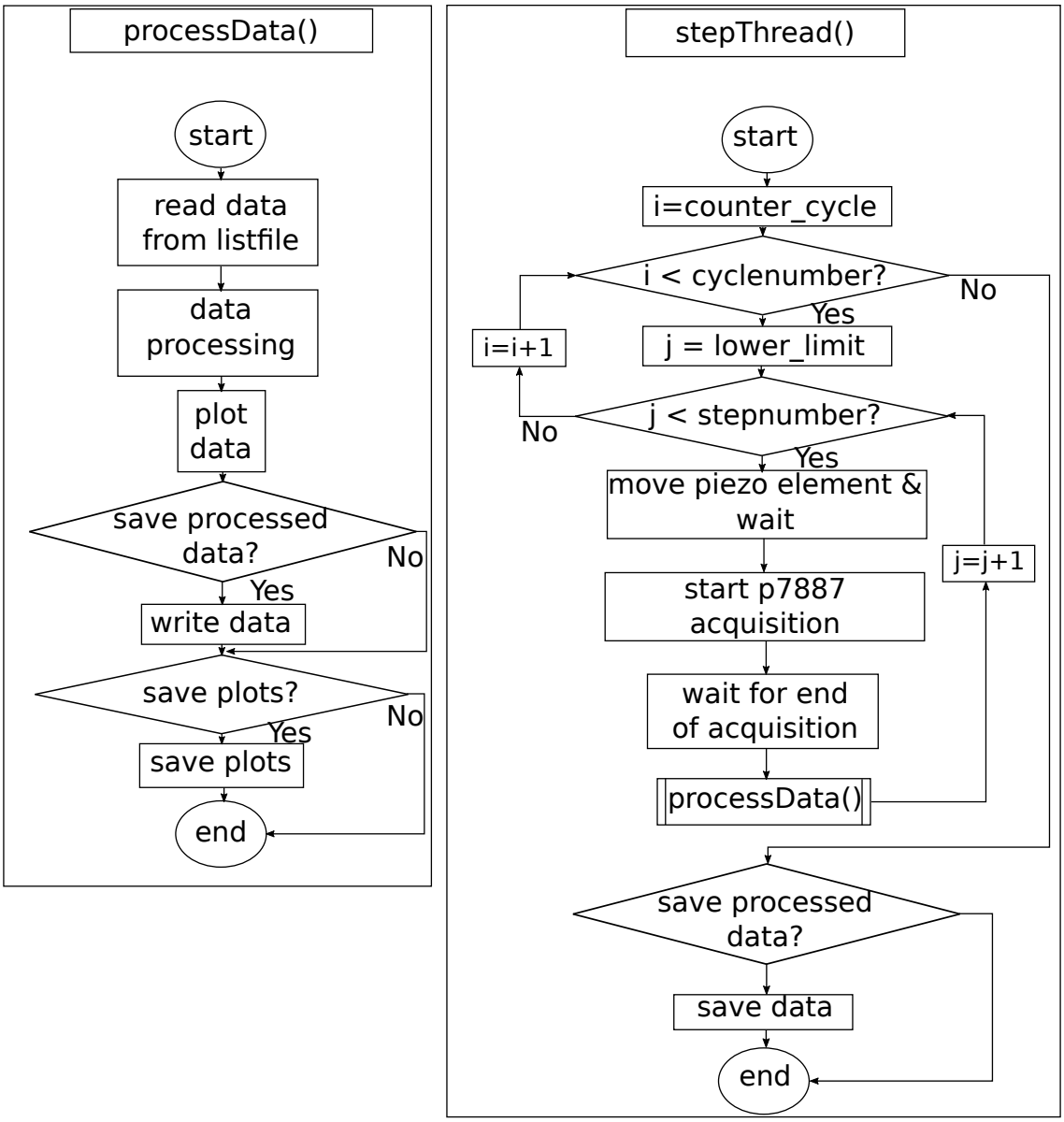

Figure 5.3: Flowchart for the methods stepThread() and processData().

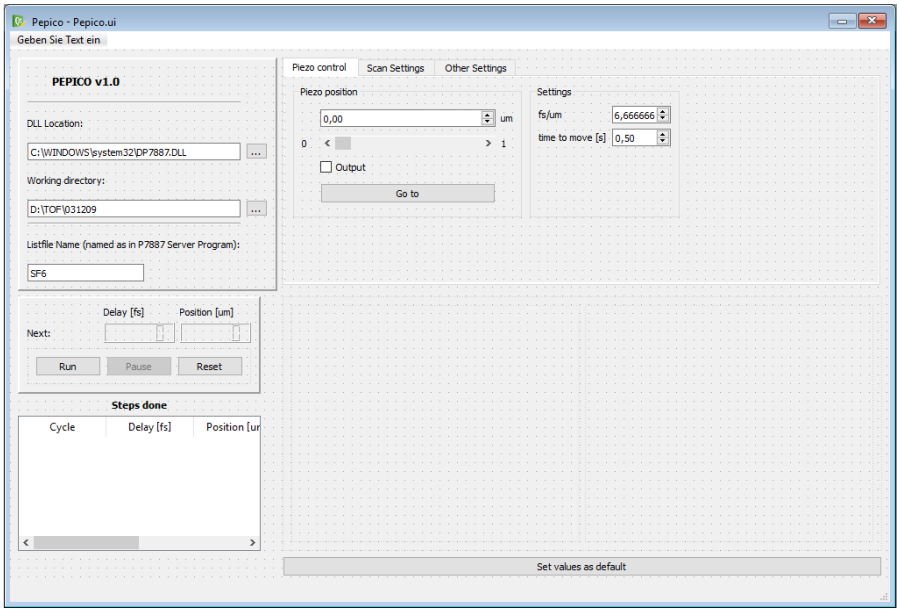

(a)

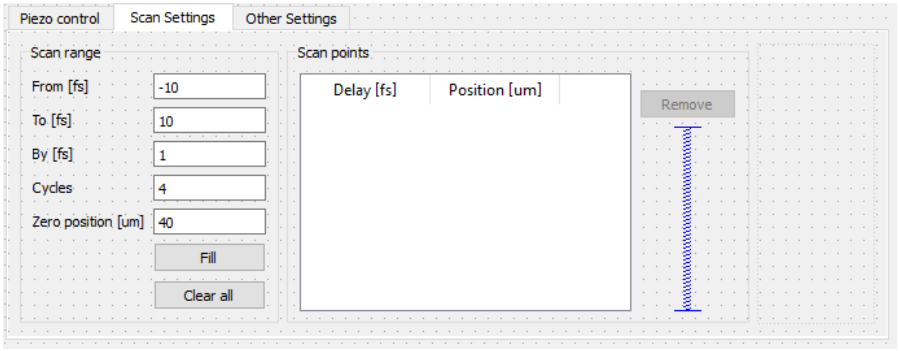

(b)

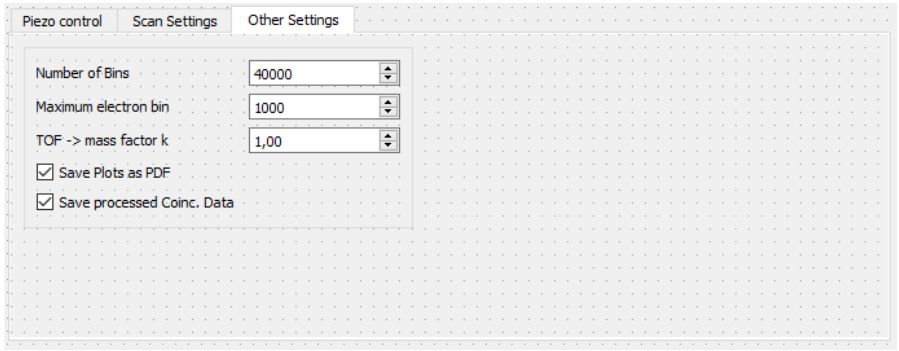

(c)

Figure 5.4: Graphical User Interface (GUI) of the Pepico program.

6 Results

6.1 Performance of the nansecond rise-time high-voltage electrical switch

The switch was driven with rectangular $5V$ pulses on the TTL inputs, provided by a pulse generator (FAST ComTec BNC Model 575) with a period of $600\mu s$. The push pulse had a pulse width of $40ns$ and the pull pulse was delayed by $\approx 30\mu s$ relative to the push pulse and had a pulse width of $50\mu s$ for ensuring full discharge of the output to ground. The output waveform depends strongly on the load and has been measured in idle state, with an unterminated transmission line connection to the plate and a terminated transmission line connection to the repeller plate, see Fig. 6.1. The transmission line consists of a $30cm$ RG58 coaxial cable with SHV connectors, which connects the switch with the experimental chamber, in series with a $\approx 1m$ copper wire, which leads to the plate.

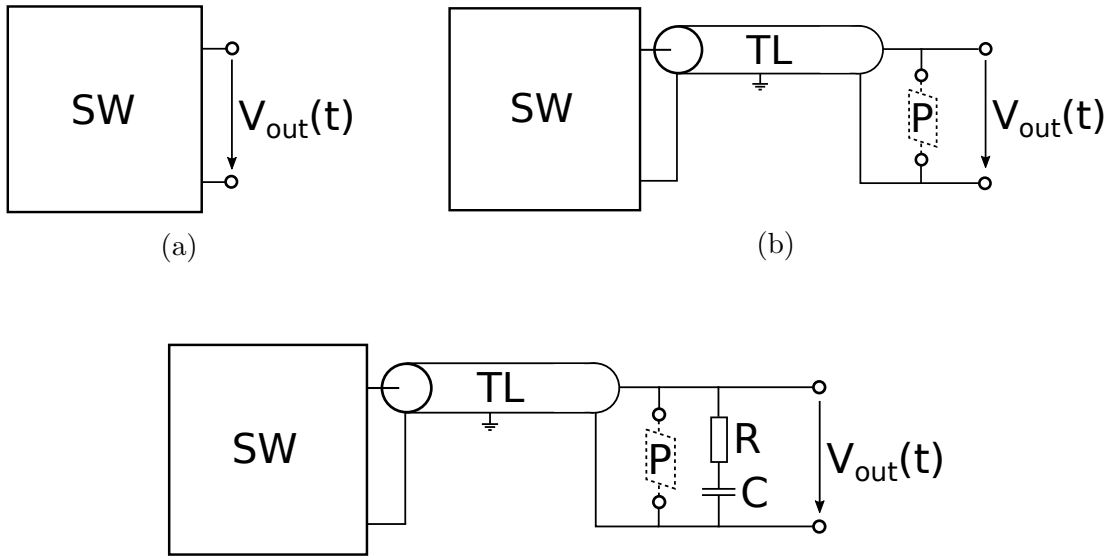

Figure 6.1: Connection schemes when measuring the output waveform. (a) Idling output of the switch SW. (b) Connection of the switch SW via an unterminated transmission line TL to the repeller plate P. (c) Connection of the switch SW via a transmission line TL, which was terminated with an RC network, to the repeller plate P.

The voltages have been measured with a digital oscilloscope (Keysight InfiniiVision DSOX2022A) and a 100:1 probe tip.

6.1.1 Output waveform in idle state at the output

The rising edge in idle state at the output can be seen in Fig. 6.2. Significant features are a very steep and clean transition with a short rise time t_R of $8.125ns$, which is primarily given by the rise time of the transistors, which is $7.7ns$ according to [36].

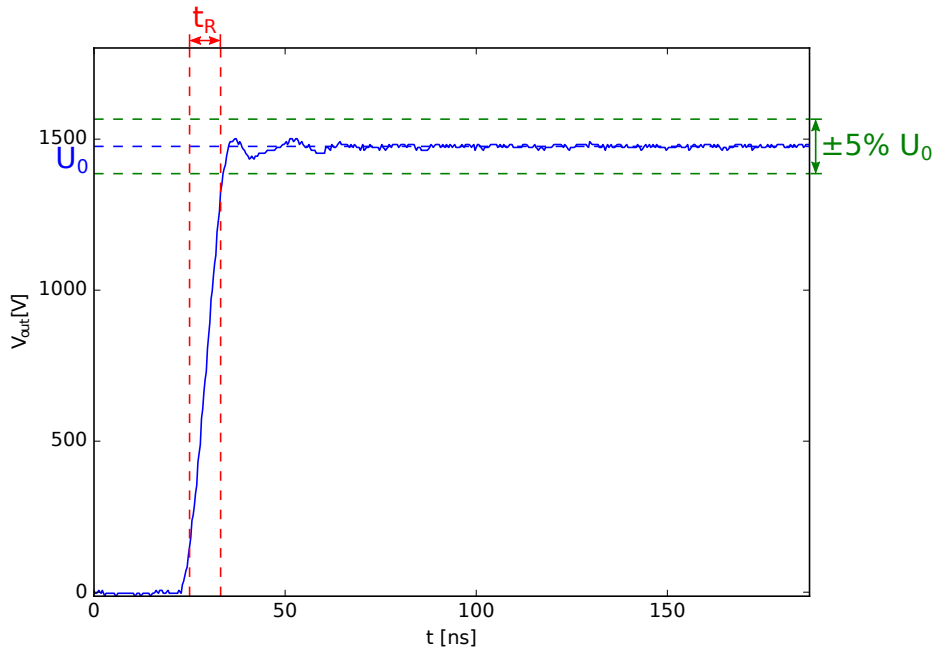

Figure 6.2: Rising edge from $0V$ to $U_0 \approx 1370V$ of the high-voltage electrical switch in idle state at the output.

The measured output voltage, including the rising- and falling-edge, can be seen in Fig. 6.3. The output voltage remains constant for the on-time t_{on} of the high-side of the switch, which can be set by the resistor R_{bias} (see Fig. 4.3). Then, the transistors on the push-side of the switch open, so the load capacity starts to discharge until the pull-side of the switch turns on and pulls the output to ground within the fall time t_f. Measured values for the on-time t_{on} and for the fall-time t_f can also be seen in table 6.1.

The offset voltage V_{off} couldn't be detected within the accuracy of the measurement with the oscilloscope, because it was too low. However, an offset voltage V_{off} would be detected by a constant energy-shift in the photoelectron spectra, which was also not the case (see ch. 6.2.1).

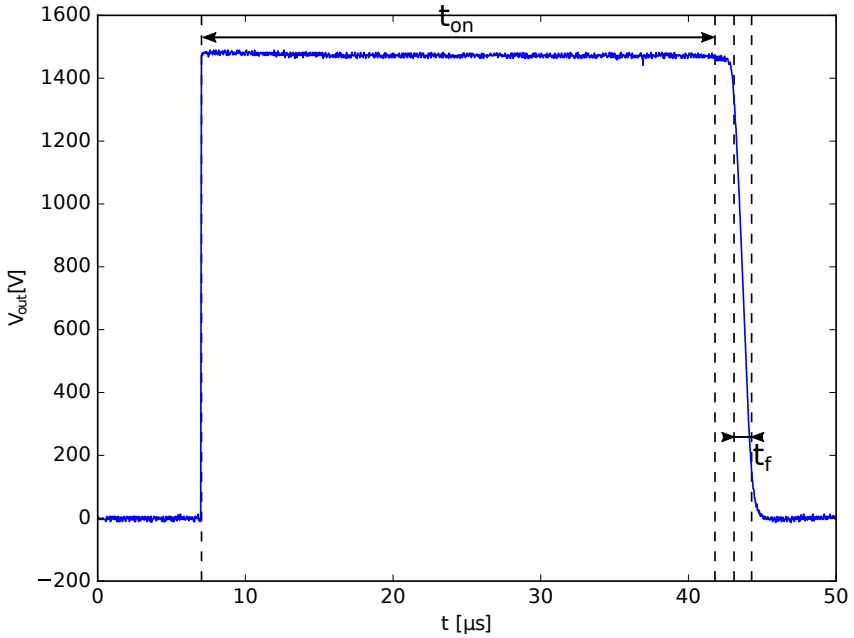

Figure 6.3: Measured output voltage of the switch including the rising- and the falling edge with an unterminated connection to the repeller plate.

t_R	$8.125ns$
t_{on}	$34.8\mu s$
t_f	$1.19\mu s$
U_0	$1476V$

Table 6.1: Measured characteristic values for the output waveform $V_{out}(t)$ of the high-voltage electrical switch with an unterminated connection to the repeller plate.

6.1.2 Unterminated connection to the repeller plate

The rising edge and the full waveform can be seen in Fig. 6.4 and in Fig. 6.5, respectively. An overshoot up to $U_0 + \Delta U_{peak}$ is clearly visible, which is followed by a transient oscillation. Due to the oscillation, the settling time t_{set} must be considered, which is defined by the time between the start of the switching process and the time when the output voltage stays in a tolerance band $\pm 5\% U_0$. Measured values of rise time t_R, overshoot ΔU_{peak} and settling time t_{set} can be seen in table 6.2. The oscillation has a period of $T \approx 26.6ns$. With the signal velocity v of $(2/3)c_0$ of an RG58 coaxial cable, with c_0 being the vaccum speed of light, it can be shown by calculation that the oscillations are due to reflexions on the transmission line of length

$$l = \frac{1}{2}\frac{2c_0}{3}T = 1.65m. \tag{6.1}$$

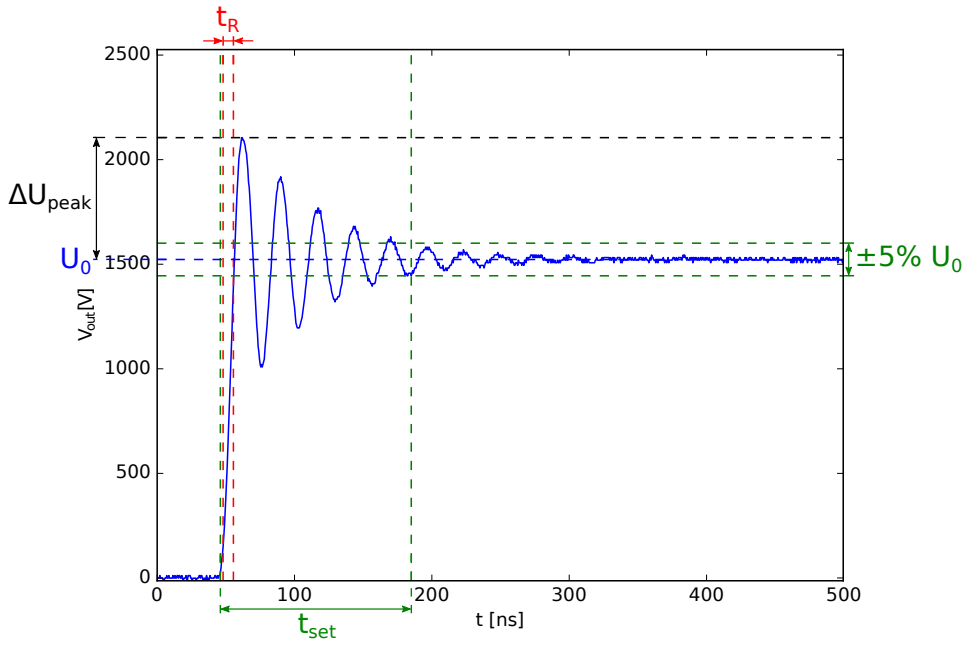

Figure 6.4: Rising edge from $0V$ to $U_0 \approx 1500V$ of the high-voltage electrical switch with an unterminated connection to the repeller plate.

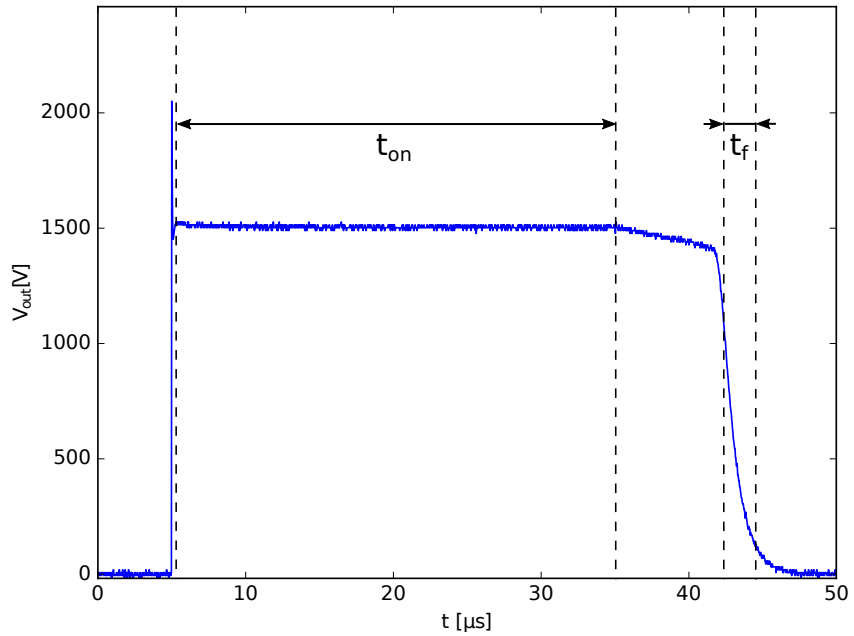

Figure 6.5: Measured output voltage of the switch including the rising- and the falling edge with an unterminated connection to the repeller plate.

t_R	$7.5ns$
t_{set}	$139ns$
t_{on}	$29.8\mu s$
t_f	$2.2\mu s$
U_0	$1522.7V$
$\frac{\Delta U_{peak}}{U_0}$	38.3%

Table 6.2: Measured characteristic values for the output waveform $V_{out}(t)$ of the high-voltage electrical switch with an unterminated connection to the repeller plate.

6.1.3 Terminated connection to the repeller plate

Oscillations in the output waveform after the rising edge could strongly reduce the mass resolution in PEPICO measurements. In order to avoid oscillations, the transmission line has been terminated with an RC network. An optimal waveform has been measured with a resistance of $R = 120\Omega$. The capacity C has been chosen to be $1nF$, such that the RC time constant $\tau = RC$ is in the order of the settling time $t_{set} = 139ns$ of the unterminated output waveform. The reason for not choosing a purely resistive line termination is the high average power consumption

$$P_{av,R} \approx \frac{U_0^2}{R} \cdot \frac{30\mu s}{600\mu s} = 416.67W \tag{6.2}$$

of such a line termination. With an RC line termination, the RC network only consumes an average power $P_{av,RC}$ of

$$P_{av,RC} = P_{av,RC,R} + P_{av,RC,C} \approx \frac{U_0^2}{R} \cdot \frac{\tau}{600\mu s} + \frac{1}{2} C U_0^2 \frac{1}{600\mu s} = 2.5W, \tag{6.3}$$

which consists of the power consumed by the resistor $P_{av,RC,R}$ and the power $P_{av,RC,C}$ consumed by charging the capacitor as many times as dictated by the repetition rate of switching. Because of the power consumption of the RC network, the average power consumption is increased by $2.5W$ compared to the unterminated transmission line. That is why the supply voltage U_0 had to be reduced, due to the limited output power of the provided high-voltage supply in the laboratory.

The rising edge can be seen in Fig. 6.6. Compared to the waveform of the unterminated connection (see Fig. 6.4), the oscillation of the signal has been reduced strongly and it resembles the rising edge in idle state (see Fig. 6.2) well, also the rise time t_R is the same as in idle state. There is still some oscillation with a period of $T \approx 14.5ns$, which could come either from reflexions or from induction, since this oscillation drifts slightly when changing the orientation of the probe tip. There is no overshoot within the 5% tolerance band and the settling time t_{set} has also decreased compared to the unterminated connection.

The measured output voltage waveform including both, the rising- and the falling edge can be seen in Fig. 6.7. The fall time t_f is much longer at lower voltage U_0, which is due to the circuit design of the pull-side (see ch. 4.2.2), but still short enough for full discharge to ground until the next pulse.

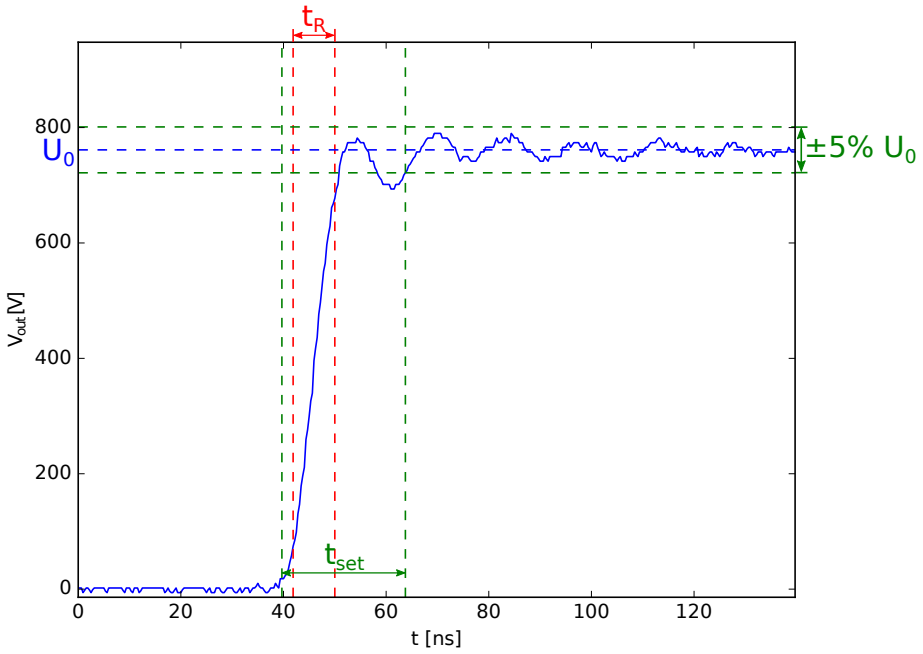

Figure 6.6: Rising edge from $0V$ to $U_0 \approx 788V$ of the high-voltage electrical switch with a terminated connection to the repeller plate.

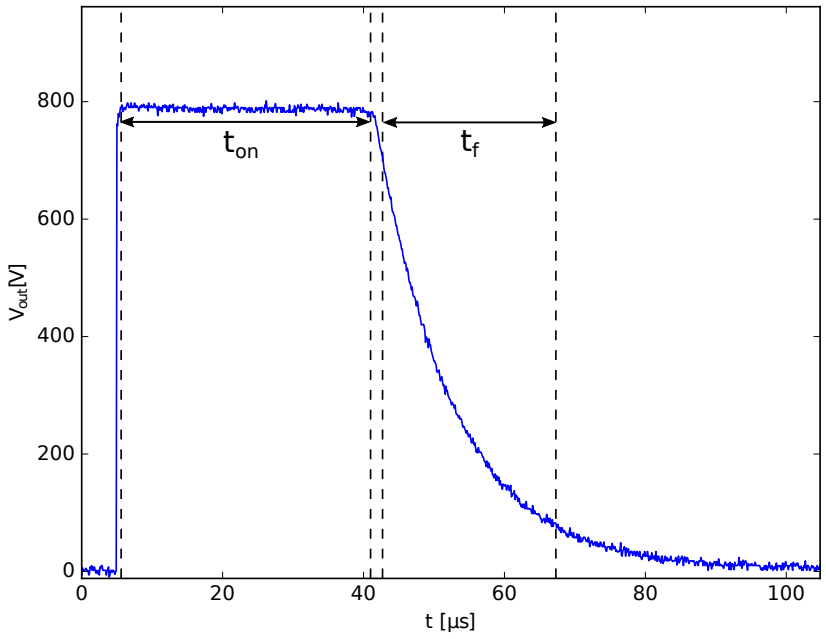

Figure 6.7: Measured output voltage of the switch including the rising- and the falling edge with a terminated connection to the repeller plate.

t_R	$8.125ns$
t_{set}	$24.0625ns$
t_{on}	$35.4\mu s$
t_f	$24.6\mu s$
U_0	$788V$

Table 6.3: Measured characteristic values for the output waveform $V_{out}(t)$ of the high-voltage electrical switch with a terminated connection to the repeller plate.

6.2 PEPICO measurements

In this section, the results of testing the possibility for PEPICO measurements with the nanosecond high-voltage electrical in the experimental chamber will be presented. The requirements for PEPICO measurements are:

- The photoelectron spectrum is not affected by the switched voltage applied to the repeller plate.
- The ionic fragments can be distinguished from each other in the photoion spectrum.

Since the former requirement can be fulfilled by switching the voltage after the longest time-of-flight of photoelectrons, the latter requirement can only be fulfilled when switching the voltage not too late after ionization, since the ionic peaks broaden due to coulomb repulsion the longer the switching delay. For test measurements photoelectron- and photoion spectra of Krypton have been measured.

During acquisition of the data, which will be presented in this chapter, the IR pulse energy was about $170\mu J$ and the vacuum in the experimental chamber was about $5.5 \cdot 10^{-6} mbar$. Since both, electrons and ions needed to be detected at the same time, the count rate, which can be achieved, is lower in comparison to measurements were only electrons or ions need to be detected. This is, because the optimal adjustment of the experimental parameters, which are needle position, MCP voltages, position of the IR focus, alignment of the laser and target gas flux, is not the same for electrons and for ions. Proper adjustment of the experimental parameters yielded a count rate of $30 cts/s$ for each, photoelectrons and photoions.

6.2.1 Effect of the switching voltage on the photoelectron spectrum

For determining the effect of the switched voltage on the photoelectrons, the photoelectron spectrum was measured with and without switching, which can be seen in Fig. 6.8. The switching induced a very strong signal between $0.82\mu s$ and $1.27\mu s$ after ionization. The photoelectron spectrum in this range cannot be recovered, which is why it is cut in this range in case of switching in Fig. 6.8(b). However, photoelectrons, which are detected before the switching, are not affected by the switching within accuracy of the measurement.

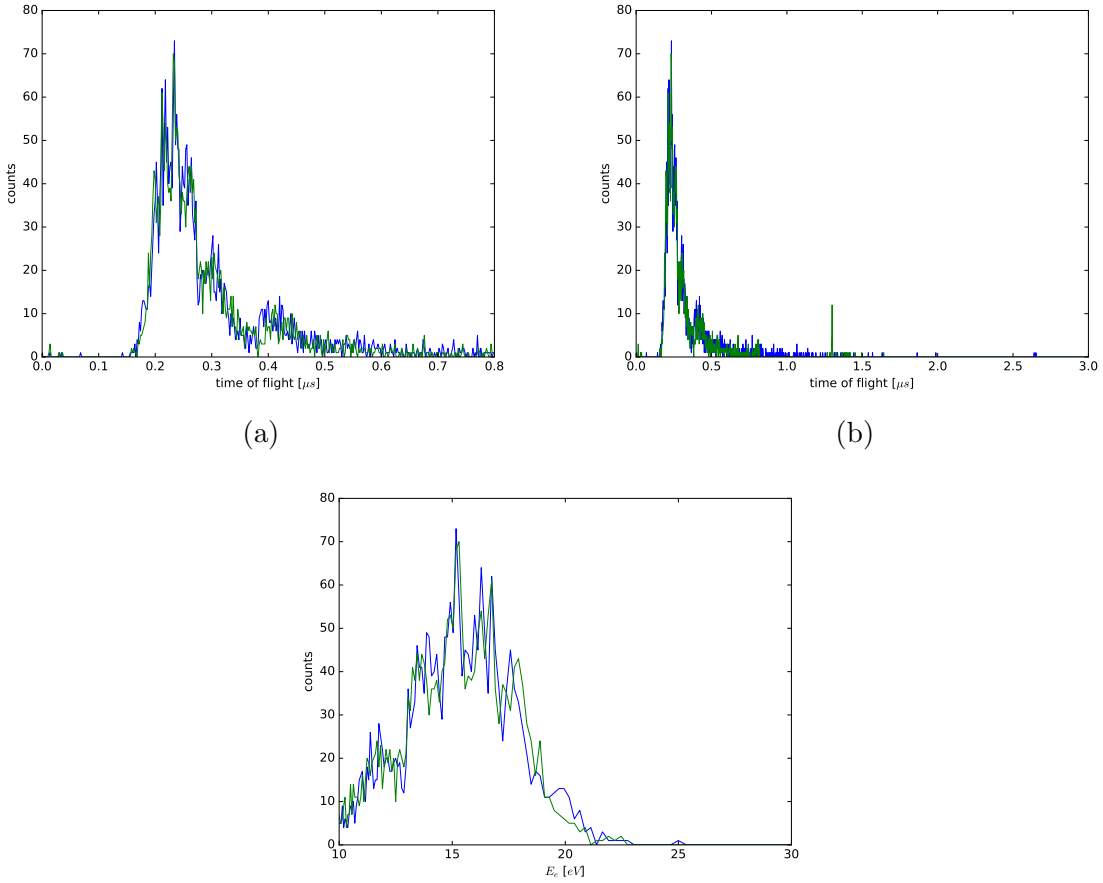

Figure 6.8: Photoelectron spectrum of Kr measured with switching at $820ns$ depending on (a), (b) the time-of-flight and (c) on photoelectron energy E_e. Blue: without switching, Green: with switching

6.2.2 Effect of the switching voltage on the photoion spectrum

In order to investigate the effect of the switched voltage on the photoions, the photoion spectrum of Krypton was measured with a short and a long delay after the pulse. These spectra will be compared with the photoion spectrum measured with a static repeller voltage. Krypton shows a photoion spectrum, which includes traces of singly charged ions, coming from isotopes ^{80}Kr, ^{82}Kr, ^{83}Kr, ^{84}Kr and ^{86}Kr. As a measure for the mass resolution of the measurements, the IUPAC mass resolution definition [37] has been used, together with the relationship

$$\frac{m}{\Delta m} = \frac{1}{2}\frac{t_{TOF}}{\Delta t_{TOF}} \tag{6.4}$$

between ion mass m, the FWHM width Δm of the ion peak, the peak time-of-flight

t_{TOF} and the FWHM time-of-flight width Δt_{TOF} has been used.

Photoion Spectrum without switching

The measured photoion spectrum of Krypton can be seen in Fig. 6.9. In the full photoion spectrum, the Kr signal is clearly visible at $t \lesssim 10\mu s$, together with a duplication $\approx 200ns$ later. It shows the peaks of isotopic ions, with time-of-flight t_{TOF} and width Δt_{TOF} (FWHM) given in table 6.5.

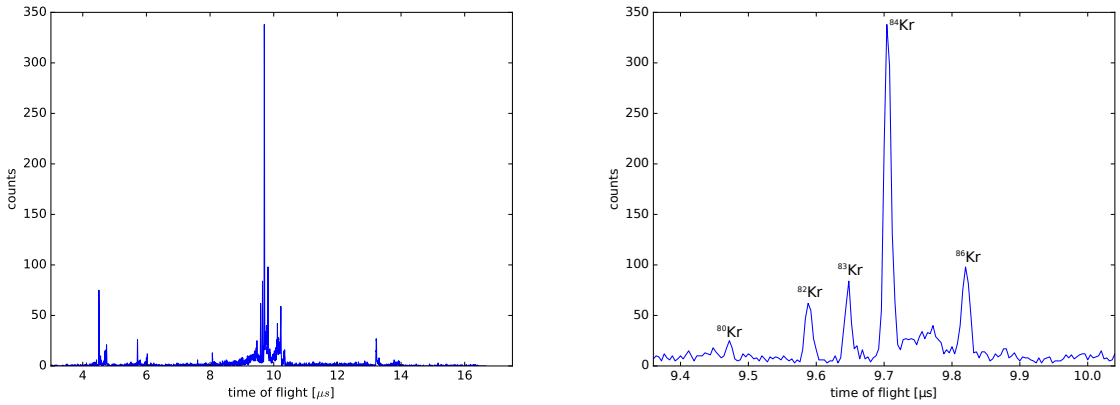

(a) (b)

Figure 6.9: Photoion spectrum depending on the time-of-flight with a voltage $U_0 = 950V$ applied to the repeller plate. (a) full photoion spectrum (b) Kr signal in the photoion spectrum

Isotope	$t_{TOF}[\mu s]$	$\Delta t_{TOF}(FWHM)[\mu s]$	$m/\Delta m$	${}^{x}Kr/{}^{84}Kr\ (peak)\ [\%]$
${}^{80}Kr$	9.47	0.015	315.67	7.7
${}^{82}Kr$	9.59	0.015	319.67	18.3
${}^{83}Kr$	9.65	0.01	482.5	25
${}^{84}Kr$	9.7	0.011	440.9	–
${}^{86}Kr$	9.82	0.015	327.3	28.9
$m/\Delta m = 377.21 \pm 70.33$				

Table 6.4: Measured characteristics of the measured photoion spectrum of Kr with a voltage $U_0 = 950V$ applied to the repeller plate.

Photoion spectrum with switching at 420ns after ionization

Fig. 6.10 shows the photoion spectrum, measured with the TOF spectrometer, when switching the voltage U_0 applied to the repeller plate from $0V$ to $950V$, with a delay of $\approx 420ns$ after ionization. This value of the delay was chosen, because it would still be late enough, such that higher energetic photoelectrons, especially those produced by XUV ionization, could be detected.

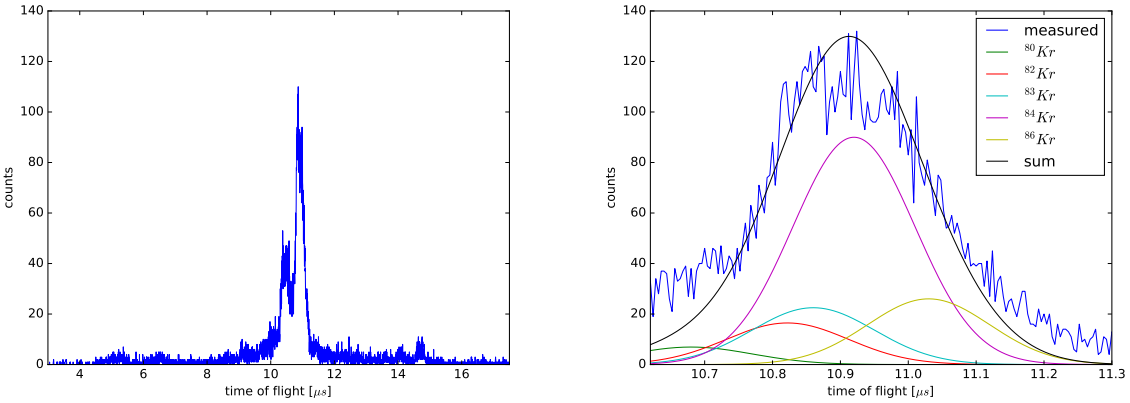

(a) (b)

Figure 6.10: Photoion spectrum measured with switching the voltage applied to the repeller plate from $0V$ to $950V$, with a delay of $\approx 420ns$ after ionization. (a) full photoion spectrum (b) Kr signal in the photoion spectrum

In Fig. 6.10 (a) the full photoion spectrum can be seen. It shows a broadening of the ion peaks, probably due to coulomb-repulsion during the switching delay. The peak of Kr, together with a duplication, can be seen at $t \gtrsim 10\mu s$, with the later peak being stronger this time. In Fig. 6.10 (b) the stronger Kr signal can be seen. The measured curve can be explained as a sum of the broadened isotopic peaks, which were fitted by Gaussian curves

$$f_i(t) = f_{i,0} \exp\left(-\frac{(t - t_{i,TOF})^2}{2\sigma^2}\right), \tag{6.5}$$

with a standard deviation $\sigma = 0.09\mu s$ for every isotope and peak counts $f_{i,0}$, which were determined such that the relative peak counts of the isotopes are identical to the measured values in table 6.5. The determined standard deviation $\sigma = 0.09\mu s$ corresponds to a FWHM peak width of

$$\Delta t_{TOF}(FWHM) = 2\sigma\sqrt{-2ln(\frac{1}{2})} = 0.106\mu s. \tag{6.6}$$

Isotope	$t_{TOF}[\mu s]$	$\Delta t_{TOF}(FWHM)[\mu s]$	$m/\Delta m$	${}^{x}Kr/{}^{84}Kr(peak)[\%]$
${}^{80}Kr$	10.68	0.212	25.19	7.7
${}^{82}Kr$	10.822	0.212	25.52	18.3
${}^{83}Kr$	10.86	0.212	25.61	25
${}^{84}Kr$	10.92	0.212	25.75	–
${}^{86}Kr$	11.03	0.212	26.01	28.9
$m/\Delta m = 25.61 \pm 0.27$				

Table 6.5: Characteristics of the measured photoion spectrum of Krypton with switching the voltage applied to the repeller plate from $0V$ to $950V$, with a delay of $\approx 420ns$ after ionization.

Photoion spectrum with switching at 820ns after ionization

Fig. 6.11 shows the measurement with a switching delay of $820ns$ after ionization. The photoion spectrum in Fig 6.11 (a) shows strongly broadened double peaks for Krypton at $t \gtrsim 11\mu s$. The stronger Krypton signal, together with a Gaussian fit (Equ. 6.5) can be seen in Fig. 6.11 (b). The signal-to-noise ratio is already very low and the isotopic peaks cannot be distinguished from each other. The Gaussian fit has a standard deviation of $\sigma = 0.442\mu s$, which corresponds to a peak width Δt_{TOF} $(FWHM)$ of $1.04\mu s$. The maximum of the fit is at $11.34\mu s$, which would give, together with Δt_{TOF} $(FWHM)$ a resolution of

$$\frac{m}{\Delta m} = 5.45. \tag{6.7}$$

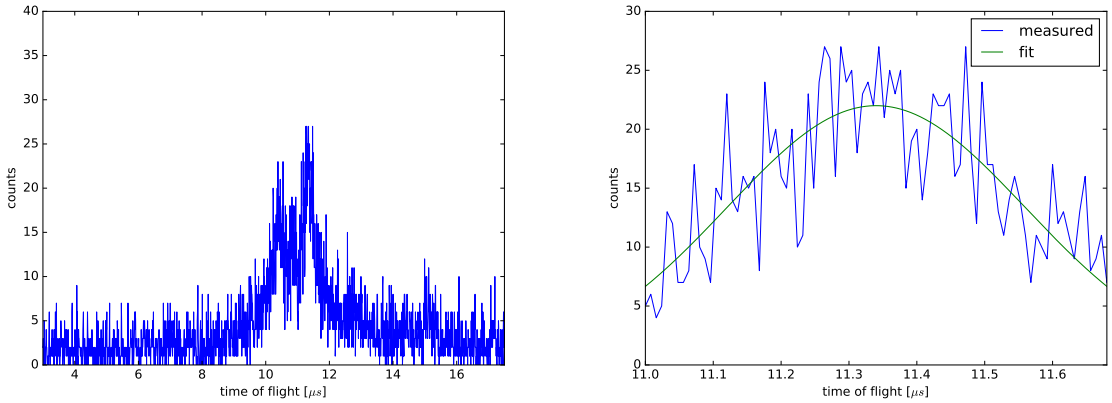

(a) (b)

Figure 6.11: Photoion spectrum measured with switching the voltage applied to the repeller plate from $0V$ to $950V$, with a delay of $\approx 820ns$ after ionization. (a) full photoion spectrum (b) Kr signal in the photoion spectrum

6.2.3 Coincidences of Kr with switching at 420ns after ionization

From the measurement, described in ch. 6.2.2, the photoelectron spectrum is shown in Fig. 6.12. As can be seen in Fig. 6.12(a), most parts of the spectrum could still be measured for a delay of $420ns$, with a mass resolution $m/\Delta m$ of ≈ 25.61. In Fig. 6.13, the PEPICO spectrum can be seen. The photoelectron spectrum is restricted to photoelectrons with a time-of-flight $t_{TOF} < 420ns$. The mass resolution was not enough to resolve the photoelectron spectra from the isotopes of Krypton, which requires the possibility to distinguish ions with masses, which are separated by $\Delta m = 1u$, at $m_{Kr84} = 127.056u$. Therefore a mass resolution $m/\Delta m$ of 127.056 would be required, whereas in the measurement a mass resolution $m/\Delta m$ of 25.61 was achieved.

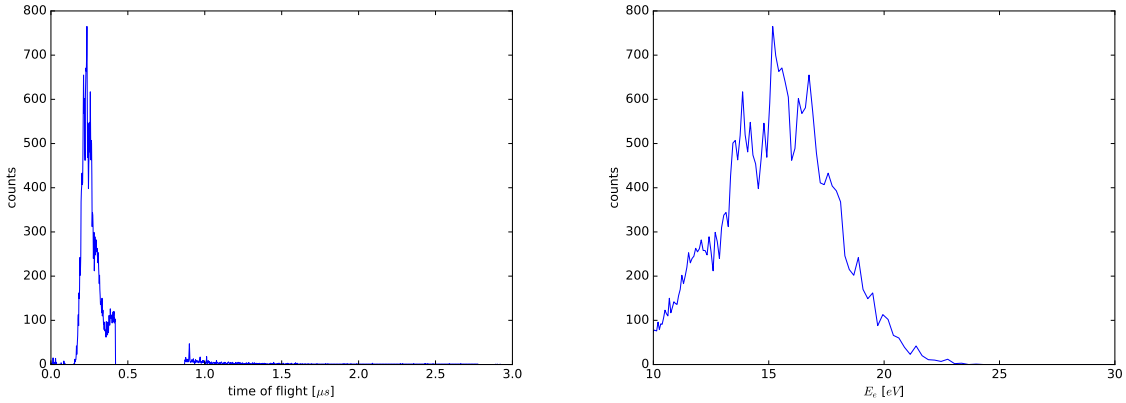

(a) (b)

Figure 6.12: Measured photoelectron spectrum of Krypton with switching the voltage applied to the repeller plate from $0V$ to $950V$, with a delay of $\approx 420ns$ after ionization depending (a) on photoelectron time-of-flight and (b) on photoelectron energy E_e.

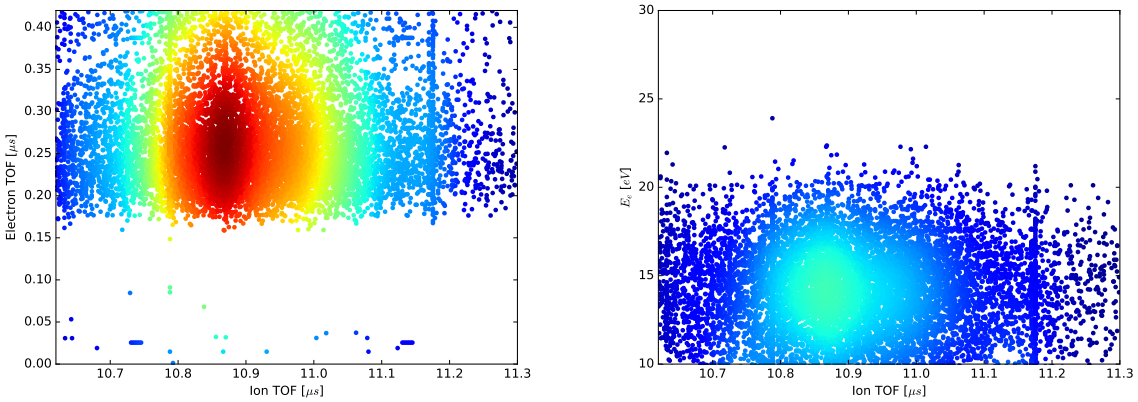

(a) (b)

Figure 6.13: Measured PEPICO spectrum of Krypton with switching the voltage U_0 applied to the repeller plate from $0V$ to $950V$, with a delay of $\approx 420ns$ after ionization depending (a) on photoion time-of-flight and photoelectron time-of-flight and (b) on photoion time-of-flight and photoelectron energy E_e.

7 Conclusions

The benefits of PEPICO spectroscopy have initiated motivation for implementing and testing the possibility for PEPICO measurements in an already existing experimental chamber of an attosecond XUV beamline, equipped with only a single time-of-flight spectrometer. Due to the high requirements regarding voltage level and rise time, which, by knowledge of the author, cannot be fulfilled with a single power MOSFET commercially available, a nanosecond rise-time high-voltage electrical switch was developed, which provides a fast, low-noise turn on of the repeller voltage, enabling the coincident detection of photoelectrons and photoions. A PEPICO software was written, which is able to coordinate the experiment and the acquisition of data, when performing time-resolved measurements. Test measurements with ionization of Krypton were performed using IR pulses, which give a strong signal and therefore, provide simple and efficient testing conditions. When testing PEPICO in the experimental chamber, it was found, that the resolution of photoions is diminished, depending on the time delay between ionization and switching of the repeller voltage. This leads to the case, that a trade off between the possibility to detect low energetic photoelectrons (demanding a long delay) and the resolution of the photoion spectrum (demanding a short delay) needs to be found. However, if such a trade off can be found for the sample under investigation, the implemented method provides a cheap possibility to perform time-resolved PEPICO measurements in an attosecond XUV beamline.

Improvements could be done regarding count rate and mass resolution. The count rate could be raised by optimizing the electric field configuration in order to enhance the collection efficiency of photoions, by adding additional electrostatic lenses or vary the geometrical shape of the repeller plate. Since the mass resolution is strongly dependent of the switching delay, ways to reduce the switching delay without affecting the photoelectron spectrum could be found. One way would be applying a negative voltage on the repeller plate before switching, which would reduce the time-of-flight of photoelectrons.

Bibliography

[1] T. Gaumnitz, A. Jain, Y. Pertot, M. Huppert, I. Jordan, F. Ardana-Lamas, and J. Wörner. Streaking of 43-attosecond soft-x-ray pulses generated by a passively cep-stable mid-infrared driver. *Opt. Express*, 25:27506–27518, 2017.

[2] M. Chini, K. Zhao, and Z. Chang. The generation, characterization and applications of broadband isolated attosecond pulses. *Nat. Photonics*, 8:178–186, 2014.

[3] F. Lépine, M.Y. Ivanov, and M. J. J. Vrakking. Attosecond molecular dynamics: fact of fiction? *Nat. Photonics*, 8:195–204, 2014.

[4] F. Krausz and M. I. Stockman. Attosecond metrology: from electron capture to future signal processing. *Nat. Photonics*, 8:205–213, 2014.

[5] Ahmed H. Zewail. Femtochemistry: Atomic-scale dynamics of the chemical bond. *J. Phys. Chem. A*, 104:5660–5694, 2000.

[6] A. Schiffrin et al. Optical-field-induced current in dielectrics. *Nature*, 493:70–74, 2013.

[7] M. Koch, P. Heim, B. Thaler, M. Kitzler, and W. E. Ernst. Direct observation of a photochemical activation energy: a case study of acetone photodissociation. *J. Phys. B: At. Mol. Opt. Phys*, 50:125102, 2017.

[8] E. Gagnon, P. Ranitovic, X.-M. Tong, C. L. Cocke, H. C. Murnane, M. M. Kapteyn, and A. S. Sandhu. Soft x-ray-driven femtosecond molecular dynamics. *Science*, 317:1374–1378, 2007.

[9] A. S. Sandhu, E. Gagnon, R. Santra, V. Sharma, and W. Li. Observing the creation of electronic feshbach resonances in soft x-ray-induced o_2 dissociation. *Science*, 322:1081–1085, 2008.

[10] Vinzenz Stummer. Active laser beam pointing stabilization for the generation of broadband optical spectra. Bachelor thesis, Photonics Institute, TU Wien, 2016.

[11] Rp photonics: Kerr lens mode locking. `https://www.rp-photonics.com/kerr_lens_mode_locking.html?s=ak`. Accessed: 2018-03-28.

[12] Rp photonics: Mode locking. `https://www.rp-photonics.com/mode_locking.html?s=ak`. Accessed: 2018-03-28.

[13] Rp photonics: Chirped-pulse amplification. `https://www.rp-photonics.com/chirped_pulse_amplification.html`. Accessed: 2018-05-03.

[14] S. De Silvestri, M. Nisoli, and O. Svelto. Generation of high energy 10 fs pulses by a new pulse compression technique. *Appl. Phys. Lett.*, 68:2793–2795, 1996.

[15] A. McPherson, G. Gibson, H. Jara, U. Johann, T. S. Luk, I. A. McIntyre, K. Boyer, and C. K. Rhodes. Studies of multiphoton production of vacuum-ultraviolet radiation in the rare gases. *J. Opt. Soc. Am. B*, 4:595–601, 1987.

[16] K. Midorikawa. High-order harmonic generation and attosecond science. *Jpn. J. Appl. Phys.*, 50:090001, 2011.

[17] Wikipedia: Extreme ultraviolet. `https://en.wikipedia.org/wiki/Extreme_ultraviolet`. Accessed: 2018-03-29.

[18] K. J. Schafer, B. Yang, L. F. DiMauro, and K. C. Kulander. Above threshold ionization beyond the high harmonic cutoff. *Phys. Rev. Lett.*, 70:1599–1602, 1993.

[19] P. B. Corkum. Plasma perspective on strong field multiphoton ionization. *Phys. Rev. Lett.*, 71:1994–1997, 1993.

[20] J. L. Krause, K. J. Schafer, and K. C. Kulander. High-order harmonic generation from atoms and ions in the high intensity regime. *Phys. Rev. Lett.*, 68:3535–3538, 1992.

[21] W. Zhang. Angle-resolved photoemission spectroscopy. In *Photoemission Spectroscopy on High Temperature Superconductor*, chapter 2. Springer-Verlag, 2013.

[22] M. Kirchner. Time-resolved spectroscopy of molecular dynamics with xuv pulses. Master's thesis, Photonics Institute, TU Wien, 2017.

[23] F. Krausz and M. Ivanov. Attosecond physics. *Rev. Mod. Phys*, 81:163–234, 2009.

[24] T. A. Carlson and M. O. Krause. Atomic readjustment to vacancies in the k and l shells of argon*. *Phys. Rev. Lett.*, 137:A1655–A1662, 1965.

[25] A. Migdal. Ionization of atoms accompanying α- and β-decay. *J. Phys. Acad. Sci. USSR*, 4:449–453, 1941.

[26] B. H. Bransden and C. J. Joachain. *Physics of atoms and molecules*. Longman Scientific & Technical, 1983.

[27] P. Krehl and S. Engemann. August toepler - the first who visualized shock waves. *Shock Waves*, 5:1–18, 1995.

[28] G. Wu, P. Hockett, and A. Stolow. Time-resolved photoelectron spectroscopy: from wavepackets to observables. *Phys. Chem. Chem. Phys*, 13:18447–18467, 2011.

[29] C. D. Lin. *Review of Fundamental Processes and Applications of Atoms and Ions*. World Scientific, 1993.

[30] T. E. Sharp. Potential-energy curves for molecular hydrogen and its ions. *Atomic Data*, 2:119–169, 1971.

[31] X.-W. Feng, X.-W. Long, and Z.-Q. Tan. Nanosecond square high voltage pulse generator for electro-optic switch. *Rev. Sci. Instrum.*, 82:075102, 2011.

[32] Transistor–transistor logic. `https://en.wikipedia.org/wiki/Transistor%E2%80%93transistor_logic`. Accessed: 2018-04-03.

[33] P. Horowitz. *The Art of Electronics, 3rd Edition*. Cambridge University Press, 2015.

[34] Texas Instruments. *LM2595 SIMPLE SWITCHER® Power Converter 150-kHz 1-A Step-Down Voltage Regulator*.

[35] Linear Technology. *LT1082: 1A High Voltage, Efficiency Switching Voltage Regulator*.

[36] STMicroelectronics. *STP5NK100Z*.

[37] Iupac goldbook-resolution in mass spectrometry. `http://goldbook.iupac.org/html/R/R05318.html`. Accessed: 2018-05-06.